



Hiding behind a curtain of dust: Gas and dust properties of an ultra-luminous strongly-lensed $z=3.75$ galaxy behind the Milky Way disc

Downloaded from: <https://research.chalmers.se>, 2026-03-03 07:00 UTC

Citation for the original published paper (version of record):

Alcalde Pampliega, B., Harrington, K., Amvrosiadis, A. et al (2026). Hiding behind a curtain of dust: Gas and dust properties of an ultra-luminous strongly-lensed $z=3.75$ galaxy behind the Milky Way disc. *Astronomy and Astrophysics*, 706.
<http://dx.doi.org/10.1051/0004-6361/202556106>

N.B. When citing this work, cite the original published paper.

Hiding behind a curtain of dust: Gas and dust properties of an ultra-luminous strongly-lensed $z = 3.75$ galaxy behind the Milky Way disc

Belén Alcalde Pampliega^{1,2,3,*}, Kevin C. Harrington^{4,5,1,2}, Aristeidis Amvrosiadis⁶, Manuel Aravena^{2,7},
Min S. Yun⁸, Hugo Messias^{1,4}, Antonio Hernán-Caballero⁹, Leindert Boogaard¹⁰, Axel Weiß¹¹,
Benjamin Beauchesne^{12,13}, Alejandro Santamaría-Miranda¹⁴, Monica Ivette Rodríguez¹⁵,
Eric Jiménez-Andrade¹⁶, Manuel Solimano², James Lowenthal¹⁷, Patrick Kamieneski¹⁸, Q. Daniel Wang⁸,
Chentao Yang¹⁹, Amit Vishwas²⁰, Pascale Hibon¹, Brenda Frye²¹, Jorge González-Lopez², Yiqing Song¹,
and Meghana Killi²

¹ ESO Vitacura, Alonso de Córdova 3107, Vitacura, Casilla 19001, Santiago de Chile, Chile

² Instituto de Estudios Astrofísicos, Facultad de Ingeniería y Ciencias, Universidad Diego Portales, Av. Ejército Libertador 441, Santiago, Chile

³ SKA Observatory, Jodrell Bank, SK11 9FT Macclesfield, UK

⁴ Joint ALMA Observatory, Alonso de Córdova 3107, Vitacura 763-0355, Santiago, Chile

⁵ National Astronomical Observatory of Japan, Los Abedules 3085 Oficina 701, Vitacura 763 0414, Santiago, Chile

⁶ Centre for Extragalactic Astronomy, Durham University, Department of Physics, South Road, Durham DH1 3LE, UK

⁷ Millenium Nucleus for Galaxies (MINGAL), Concepción, Chile

⁸ Department of Astronomy, University of Massachusetts, Amherst, MA 01003, USA

⁹ Centro de Estudios de Física del Cosmos de Aragón (CEFCA), Plaza San Juan 1, E-44001 Teruel, Spain

¹⁰ Leiden Observatory, Leiden University, P.O. Box 9513, 2300 RA Leiden, The Netherlands

¹¹ Max-Planck-Institut für Radioastronomie, Auf dem Hügel 69, 53121 Bonn, Germany

¹² Centre for Extragalactic Astronomy, Department of Physics, Durham University, South Road, Durham DH1 3LE, UK

¹³ Institute for Computational Cosmology, Durham University, South Road, Durham DH1 3LE, UK

¹⁴ Departamento de Astronomía, Universidad de Chile, Camino El Observatorio 1515, Las Condes, Santiago, Chile

¹⁵ Institut de Radioastronomie Millimétrique (IRAM), Av. Divina Pastora 7, Núcleo Central, 18012 Granada, Spain

¹⁶ Instituto de Radioastronomía y Astrofísica, Universidad Nacional Autónoma de México, Antigua Carretera a Pátzcuaro 8701, Ex-Hda. San José de la Huerta, Morelia, Michoacán C.P. 58089, México

¹⁷ Department of Astronomy, Smith College, Northampton, MA 01063, USA

¹⁸ School of Earth and Space Exploration, Arizona State University, PO Box 871404, Tempe, AZ 85287-1404, USA

¹⁹ Department of Space, Earth & Environment, Chalmers University of Technology, SE-412 96 Gothenburg, Sweden

²⁰ Cornell Centre for Astrophysics and Planetary Science, Cornell University, Space Sciences Building, Ithaca, NY 14853, USA

²¹ Steward Observatory, University of Arizona, 933 N Cherry Ave, Tucson, AZ 85721-0009, USA

Received 25 June 2025 / Accepted 5 December 2025

ABSTRACT

We present a detailed analysis of J154506, a strongly lensed submillimetre galaxy (SMG) behind the Lupus-I molecular cloud, and a characterisation of its physical properties using a combination of new and archival data, including VLT/MUSE and FORS2 optical data. We identify two high-significance ($S/N > 5$) emission lines at 97.0 and 145.5 GHz, corresponding to CO(4-3) and CO(6-5), respectively, in spectral scans from the Atacama Compact Array (ACA) and the Large Millimetre Telescope (LMT), as well as the [CII] 158 μm fine-structure line at 400 GHz observed with the Atacama Pathfinder Experiment (APEX). These detections yield a spectroscopic redshift of $z_{\text{spec}} = 3.7515 \pm 0.0005$. We also report the detection of [CI], HCN(4-3), and two H_2O^+ transitions, further confirming the redshift and providing insights into the physical properties of J154506. By modelling sub-arcsecond resolution ($0.75''$) ALMA Band 6 and 7 continuum data in the uv -plane, we derive an average magnification factor of 6.0 ± 0.4 , and our analysis reveals a relatively cold dust (38 K) in a starburst galaxy ($\sim 900 M_{\odot} \text{ yr}^{-1}$) with a high intrinsic dust mass ($\sim 2.5 \times 10^9 M_{\odot}$) and infrared (IR) luminosity ($\sim 6 \times 10^{12} L_{\odot}$). Non-local thermodynamic equilibrium radiative transfer modelling of the joint dust spectral energy distribution (SED) and CO line excitation suggests the dust continuum emission is primarily associated with relatively diffuse regions with molecular gas densities of $10^2 - 10^4 \text{ cm}^{-3}$, rather than compact, high-pressure environments typical of extreme starbursts or active galactic nuclei (AGNs). This interpretation is supported by the close-to-unity ratio between the dust and gas kinetic temperatures, which argues against highly energetic heating mechanisms. The CO excitation ladder peaks close to CO(5-4) and is dominated by slightly denser molecular gas. Our results underscore the unique power of far-IR and submillimetre observations to both uncover and characterise scarce, strongly lensed, high-redshift galaxies, even when they are obscured by foreground molecular clouds.

Key words. gravitational lensing: strong – galaxies: high-redshift – galaxies: starburst – submillimeter: galaxies

* Corresponding author: Belén.AlcaldePampliega@skao.int

1. Introduction

Over the past two decades, (sub)millimetre surveys have revolutionised our understanding of galaxy formation and evolution by revealing an unexpected population of high-redshift, dust-obscured massive galaxies with intense star formation rates (SFR), the so-called submillimetre (submm) galaxies (SMGs; see, e.g. Casey et al. 2014, for a review). Extremely bright SMGs (i.e. $S_{500\mu\text{m}} > 100\text{ mJy}$; Negrello et al. 2017) provide a unique opportunity to study the interstellar medium (ISM) of galaxies due to their high luminosity, which is often enhanced by gravitational lensing. This natural magnification enables detailed studies of star formation (SF) activity, dust, and molecular gas properties and dynamics, providing insights into the conditions that prevail in the early stages of galaxy evolution at scales and sensitivities otherwise unattainable at such distances. However, for high-redshift galaxy surveys in the so-called zone of avoidance (ZOA), this progress is hampered by Galactic absorption and contamination from Galactic brown dwarfs (e.g. Kraan-Korteweg & Lahav 2000; Woudt et al. 2004; Amôres et al. 2012; Duplancic et al. 2024). The ZOA covers $\sim 25\%$ of the distribution of optically visible galaxies and is reduced to 10–20% in IR surveys (Kraan-Korteweg & Lahav 2000; Kraan-Korteweg 2005). Because of their very red colours and point-like appearance, brown dwarfs mimic the observational properties of distant SMGs, complicating the identification and selection of genuine high-redshift sources. Furthermore, extremely bright SMGs and low-mass starless cores exhibit remarkably similar flux densities across the mid-infrared (MIR)-to-submm regime, adding another layer of complexity to disentangling these populations (e.g. Barnard et al. 2004; Wilkins et al. 2014). Studies of both local and high-redshift sources must therefore account for each other as potential sources of contamination. In fact, the unprecedented sensitivity of the James Webb Space Telescope (JWST) has led to the identification of Galactic brown dwarfs in deep, multiband imaging and spectroscopic extragalactic surveys (e.g. Nonino et al. 2023; Hainline et al. 2024; Burgasser et al. 2024).

Dust emission in a typical local galaxy peaks at wavelengths around $100\mu\text{m}$ rest-frame. At $z = 3\text{--}4$, this peak will move into the $500\mu\text{m}$ SPIRE (Spectral and Photometric Imaging Receiver, on board the Herschel Space Observatory) band (e.g. Dowell et al. 2014; Ivison et al. 2016; Clements et al. 2024). Sources whose dust emission has not reached its peak in this band will most likely lie above redshift 4 (e.g. Greenslade et al. 2019, 2020). Understanding the intrinsic physical properties of strongly lensed galaxies requires precise knowledge of the redshifts of both the lens and the background lensed galaxy. Unfortunately, the optical-near-infrared (NIR) spectroscopic confirmation of dusty red galaxies at high-redshift, often extremely red or invisible at those wavelengths, is very challenging (e.g. Alcalde Pampliega et al. 2019; Wang et al. 2019; Williams et al. 2019). This becomes increasingly difficult when the entire system is further obscured by local dust clouds within our own galaxy, as is the case for the high-redshift galaxy J154506.3-344317.9 (hereafter J154506 for brevity). As a consequence, submm spectral-scan observations targeting bright CO and [CI] emission lines, which are not affected by dust extinction and can be directly associated with the background source, represent a more efficient and widely used method that has been proven to be very successful in getting robust and unambiguous redshifts (e.g. Vieira et al. 2013; Strandet et al. 2016; Reuter et al. 2020; Neri et al. 2020; Urquhart et al. 2022; Chen et al. 2022).

Recently, sub-arcsec resolution observations with the Atacama Large Millimeter/submillimeter Array (ALMA) of pre-brown dwarf candidates in the Lupus-I molecular cloud uncovered optical-and-NIR undetected objects exhibiting far infrared (FIR) spectral energy distributions (SEDs) compatible with both young (pre)stellar objects and extragalactic sources (Santamaría-Miranda et al. 2021). Among them, J154506, located at a $12''$ distance from the target source, stands out due to its extremely bright submm flux with a SED rising up to $500\mu\text{m}$, and compelling evidence of being a strongly gravitationally lensed SMG seen through the Milky Way disc (Santamaría-Miranda et al. 2021).

In this work, we combine archival data with submm spectral scans to report the spectroscopic redshift confirmation of J154506 and provide an initial investigation of its dust and molecular gas properties. Throughout the paper, we adopt a flat Lambda cold dark matter (Λ CDM) cosmology with $H_0 = 70\text{ km s}^{-1}\text{ Mpc}^{-1}$, $\Omega_\Lambda = 0.7$, $\Omega_M = 0.3$, and a Chabrier (2003) initial mass function. All the magnitudes refer to the AB system (Oke & Gunn 1983).

2. J154506: A strongly lensed system

J154506 (RA = 15:45:06.333, Dec = $-34:43:17.972$) is a unique system located towards the Lupus-I Galactic molecular cloud in the Milky Way (at a distance of $\sim 153\text{ pc}$; e.g. Santamaría-Miranda et al. 2021). It stands out owing to its extraordinarily bright (sub)mm flux ($S_{500\mu\text{m}} = 134.4 \pm 11.9\text{ mJy}$; Tamura et al. 2015) and its extremely red $S_{250\mu\text{m}}/S_{500\mu\text{m}}$ colour (Fig. 1). Tamura et al. (2015) reported that, based on the available multiwavelength observations (unresolved at that time), J154506 was likely not a star-like source, but instead a dusty galaxy at a cosmological distance.

The far-infrared (FIR) and submm colours correlate with redshift, both empirically and theoretically (e.g. Burgarella et al. 2023; Cox et al. 2023). Figure 1 shows the $S_{870\mu\text{m}}/S_{500\mu\text{m}}$ versus $S_{250\mu\text{m}}/S_{500\mu\text{m}}$ colour-colour diagram for some of the brightest known galaxies (i.e. *Herschel*, *Planck*, and *SPT* selected sources; Harrington et al. 2016; Reuter et al. 2020; Berman et al. 2022), colour-coded by their spectroscopic redshift. There is a clear trend indicating that the brighter the source at $500\mu\text{m}$ relative to $250\mu\text{m}$, the higher its redshift tends to be. According to its position in the diagram, J154506, highlighted with a red star, is also very likely located at $z > 3$. Given that the rest-frame FIR SED typically peaks around $100\mu\text{m}$, the increase in flux density across the *Herschel* SPIRE bands for J154506 provides strong evidence for its classification as a high-redshift galaxy with extreme IR luminosity. We also note that, unlike J154506, some of the highest redshift galaxy spectral energy distributions (SEDs) continue to rise or peak nearer the observed-frame $870\mu\text{m}$. The limitations of submm colours and photometric redshifts, which provide only broad redshift ranges (as illustrated in Fig. 1), imply that precise and reliable redshift measurements require molecular and/or atomic FIR emission lines.

Initial searches for Galactic molecular lines from J154506 had limited success; any detected $^{13}\text{CO}(1\text{-}0)$ appeared homogeneous, and attempts to detect redshifted $^{12}\text{CO}(2\text{-}1)$ failed to confirm its nature (Tamura et al. 2015). While this manuscript was in preparation, Tamura et al. (2025) reported a redshift of $z = 3.753 \pm 0.001$ for J154506. Their work, based on observations with the Australian Telescope Compact Array, the Nobeyama 45 m telescope, and ALMA, identified CO(2-1), CO(4-3), and CO(9-8) emission lines. Our observations independently detected CO(4-3), CO(6-5), [CI], [CII], and other

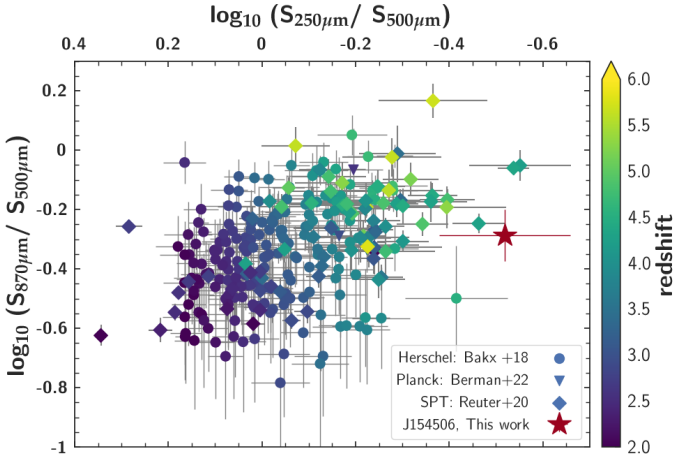


Fig. 1. Far-infrared and submm colour-colour diagram ($S_{870\mu\text{m}}/S_{500\mu\text{m}}$ vs. $S_{250\mu\text{m}}/S_{500\mu\text{m}}$), colour-coded by redshift. The brightest known sources from the *Herschel*, *Planck*, and *SPT* surveys are shown with circular, triangular, and rhomboidal symbols, respectively. J154506 is highlighted with a red star. Flux densities at $850\mu\text{m}$ (rather than at $870\mu\text{m}$) are used for the *Herschel* and *Planck* sources. The extremely red $S_{250\mu\text{m}}/S_{500\mu\text{m}}$ colour of J154506 suggests a redshift of $z > 3$.

tentative lines. This rich dataset enables a far more detailed and rigorous analysis of the gas excitation through comprehensive combined modelling of dust and CO line SEDs. Our work provides the molecular gas and dust excitation conditions, offering new insights into the cold ISM properties of this system.

3. Observational data for J154506

Star-forming regions such as the Lupus-I molecular cloud are prime targets for multi-wavelength observations, yielding a wealth of data across the electromagnetic spectrum. In the following, we describe the data used in this work for the spectroscopic confirmation and characterisation of J154506.

3.1. ALMA ancillary data

Extensive archival submm and millimetre data from both the 7 m and 12 m ALMA arrays are available for J154506 (see Table A.1). A more in-depth description of these ALMA data can be found in Santamaría-Miranda et al. (2021); here we summarise the relevant details. The data reduction, calibration, and imaging of the ALMA Band 3, 6, and 7 (B3, B6, and B7) archival data for J154506 were performed using CASA versions 5.6.1-8, 5.1.1-5, and 5.6.1-8 (McMullin et al. 2007), respectively. We combined all spectral windows to produce both a dust continuum image and a spectral cube using natural weighting for each band. We found no significant line detection (i.e. $>3\sigma$) at either the raw or binned spectral resolution (up to $\approx 100\text{ km s}^{-1}$), even after applying uv -tapering to increase the significance. This is unsurprising, as these spectral tunings were designed to target brown dwarfs within the Lupus-I molecular cloud and were instead selected to cover local CO transitions. As noted above, ALMA B6 and B7 continuum observations (IDs: 2015.1.00512.S and 2018.1.00126.S; PI: de Gregorio-Monsalvo, I.) provide sub-arcsec resolution ($0.75''$) images that reveal the existence of at least two emitting regions at the coordinates of J154506, located at the edge of the B7 primary beam (see Figs. 2 and A.1). We reimaged the B6 and B7 data using BRIGGS weighting with robust = 0.5 and 1. These images allowed us to constrain the relative

position of the foreground lens and the background galaxy with improved accuracy, and were also used to model the system in the image plane (see Section 5).

3.2. ALMA Cycle 10 Atacama Compact Array observations

The Atacama Compact Array (ACA) Cycle 10 spectral scans in Bands 3 and 4 (2023.1.00251.S; PI: Alcalde Pampliega, B.), were conducted to spectroscopically confirm the redshift of J154506. The observations consist of six observing blocks (OBs), three in each of Band 3 and Band 4 (B3 and B4), and were carried out between November 9, 2023 and January 11, 2024, with a total time on-source range of 9–18 minutes per OB. We used a total of 9–11 antennas, reaching maximum baselines ranging from 48.0 to 48.9 m and an angular resolution of 6 – $11''$. The six tunings provided continuous coverage of two frequency ranges: 90–111 and 139–162 GHz in B3 and B4, respectively. We observed 12 spectral windows, each of 1.875 GHz, with 15.6 MHz channelisation (28–53 km/s). Details of the central sky frequencies and sensitivity values are provided in Table C.1. Similar spectral setups, which maximise the likelihood of detecting two emission lines, have proven very efficient (e.g. Neri et al. 2020; Bakx & Dannerbauer 2022) in confirming the redshift of dusty high-redshift galaxies through detections of CO, [CI], and even H_2O^+ emission lines.

We performed reduction and calibration using the CASA-6.5.4-9 (CASA Team 2022) pipeline version, including visual inspections to identify and remove data with irregular amplitude or phase values. We created continuum images using the interactive TCLEAN task within CASA with natural weighting. Each spectral cube was imaged separately and cleaned using a fixed elliptical mask of $16'' \times 10''$ (major by minor axis) centred at the position of the continuum emission. During the data reduction steps, the cubes were further binned to velocity resolutions of $\approx 100\text{ km/s}$ to maximise the signal-to-noise ratio (S/N) and facilitate line detection. To mitigate contamination from potential spectral lines and account for low S/N, we initially generated no-continuum-subtracted cubes (see Fig. C.1). We subsequently measured the continuum and extracted it from line-free regions adjacent to detected emission lines. Table C.1 lists the characteristics of the final images.

3.3. Large Millimeter Telescope observations

We performed spectroscopic observations of J154506 with the 50 m Large Millimeter Telescope Alfonso Serrano (LMT; Hughes et al. 2010), in the 3 mm band using the Redshift Search Receiver (RSR; Erickson & Grosslein 2007). The LMT/RSR provides simultaneous bandwidth coverage between 73 and 111 GHz in a single tuning, with an effective beam size of $\approx 15''$. The full frequency range of the receiver is covered using six spectrometers, with sub-bands overlapping at the band edges (73.0, 79.7, 86.0, 92.1, 98.6, 104.9, and 111.0 GHz). Each band has 256 channels, with a 31.25 MHz channel width, corresponding to a velocity resolution of $\approx 100\text{ km s}^{-1}$ at 3 mm. The observations were carried out on March 4, 2024 under programme 2024-S1-MX-11 (PI: Jimenez-Andrade, E.). The total on-source time was 0.9 h, resulting in per-sub-band sensitivities of 1.05, 1.0, 0.94, 1.6, 1.12, and 1.8 mJy rms. The LMT provides science-ready data products through the standard data reduction process. For this dataset, careful data flagging was performed to increase the S/N of lower frequency tentative lines. To obtain the LMT/RSR results presented here, we applied the following gain factor, G : $G(\nu) = 2.8 \left(\frac{\nu(\text{GHz})}{100\text{ GHz}} \right) + 0.19\text{ JyK}^{-1}$.

3.4. APEX observations

We also performed observations with new FaciLity APEX Submillimeter Heterodyne instrument (nFLASH; Heyminck et al. 2006) at the Atacama Pathfinder Experiment (APEX; Güsten et al. 2006) 12 m submillimeter telescope. The nFLASH receiver has two independent dual-sideband tuneable frequency channels, nFLASH230 and nFLASH460, covering intermediate frequency (IF) ranges of 4–12 GHz and 4–8 GHz, respectively, allowing simultaneous observations in both channels. However, nFLASH460 requires much better atmospheric conditions than nFLASH230 due to the lower atmospheric transmission at higher frequencies. Therefore, the observations did not reach the requested rms. J154506 was only partially observed under the projects C-0113.F-9710C (PI: Alcalde Pampliega, B.) and C-114.F-9703C (PI: Harrington, K.). Both projects used nFLASH230 and nFLASH460 tuned to sky frequencies of 217.5 and 400 GHz, targeting [CII] and CO(9-8), respectively. The total integration times were 10.6 and 63 min (0.5 and 0.2 mK rms) for nFLASH230 and 10.6, 21.3, and 28.5 min (1.5, 1.7, and 1.5 mK rms) for nFLASH460. We reduced the APEX data using a consistent strategy, modifying the APEX template reduction script using the GREnable Graphics (GREG) and Continuum and Line Analysis Single-dish Software (CLASS) packages within Grenoble Image and Line Data Analysis Software (GILDAS)¹. We smoothed the spectrum from each scan to 40 and 100 km s⁻¹ channel resolution and averaged it after subtracting a first-order baseline from the line-free channels of all scans.

3.5. MUSE and FORS2 observations

Observations with the Multi Unit Spectroscopic Explorer (MUSE) and the FOcal Reducer and low dispersion Spectrograph 2 (FORS2) primarily aimed to confirm the redshift of the foreground lens through the detection of optical emission and absorption lines. Although J154506 was within the MUSE field of view, the probability of detecting its redshifted optical emission lines was very low. Observations were obtained as part of the ESO filler programmes 111.24UJ.009 (PI: Bian, F.) with MUSE (Bacon et al. 2010) and 111.24P0.008 (PI: Berton, M.) with FORS2, mounted at UT4 and UT1 of ESO's Very Large Telescope (VLT) at Cerro Paranal in Chile. The FORS2 spectrograph was used with the GRIS 600z+23 grism and the order separation filter OG590, providing a wavelength range of 7400–10 000 Å. The FORS2 acquisition was performed through a blind offset, and the observations consisted of ten exposures of 2700 seconds each, with the slit width set to 1.3". Due to marginal observing conditions, we could only extract spectra from five datasets. Although these were combined, we did not detect spectral features.

The MUSE instrument is an integral field unit spectrograph (R = 2000–4000) covering the 4750–9350 Å wavelength range with a 0.2" spatial resolution across a 60 × 60" field of view (i.e. the wide field mode). The MUSE observations comprised eight observing blocks (OBs), each consisting of four exposures of 700 seconds. We reduced all data using standard procedures with the ESO recipe execution tool (ESOREX). To further reduce the remaining skylines in the MUSE data, we ran the Zurich Atmosphere Purge (ZAP, Soto et al. 2016) (ZAP) sky subtraction tool. All but two of the MUSE OBs were taken under poor atmospheric conditions (i.e. thick clouds and a seeing >1"). In the

best two OBs, taken on June 21 and 19, 2023, with an airmass ≈ 1 and a seeing of 0.7 and 1.3", respectively, the lens was detected (24.5 ± 0.3 mag; see Fig. 2) but no clear line features were found. To extract the spectra, we used a circular aperture with a 1" diameter in the combined image of these two OBs. This aperture was selected to maximise the S/N after testing diameters from 0.5 to 2". The MUSE data also enabled better characterisation of the lensing galaxy position (RA = 15:45:06.441, Dec = -34:43:18.128). We aligned MUSE cubes using *Gaia*-DR3 stars within a 30"-radius circle around the source, yielding World Coordinate System (WCS) corrections smaller than 0.3". The low quality of this dataset precluded spectroscopic confirmation of the lens and prevented further detailed analysis.

4. Spectroscopic redshift confirmation

ALMA B6 and B7 sub-arcsec resolution (0.75") continuum archival observations (detailed in section 3.1) detected J154506 at the edge of the ALMA primary beam. These images resolved the continuum emission into two emitting regions: a point-like detection and a bright arc-like elongated shape (see the right panel of Fig. 2 and Fig. A.1), confirming the gravitational lensing of this extremely bright SMG.

Our ALMA Cycle 10 B3 and B4 spectral scans successfully detected two S/N ≥ 5 emission lines, at 97 and 145.5 GHz (see Fig. C.1 and bottom panels in Fig. 3), which is typically sufficient to confirm the redshift of a galaxy. However, the degeneracy in CO transitions can lead to ambiguous solutions in certain scenarios. In simple terms, multiplying the frequencies of both CO line transitions by the same integer factor can produce another valid transition, resulting in multiple possible redshifts (e.g. Bakx & Dannerbauer 2022). In this case, the lines could correspond to redshifts of 1.38, 3.75, 6.1, or 8.5. Although the ACA scans covered higher-J transitions for the potential redshifts $z = 6.12$ and 8.5, the low S/N of the spectra and the expected faintness of those transitions meant that their non-detection could not confirm the redshift. The 97 and 154 GHz lines are also compatible with the detection of CO(2-1) and CO(3-2) at $z = 1.38$; however, we discard this low redshift solution due to its incompatibility with the photometric redshift ($z_{\text{phot}} > 3$). Moreover, the derived dust temperature from FIR fitting at $z = 1.38$, $T = 15$ K is low and unlikely for galaxies at that redshift (e.g. Schreiber et al. 2018). In addition, the intrinsic SFR_{IR} would be below 100 M_⊙ yr⁻¹.

The LMT/RSR spectrum simultaneously covers the 73–111 GHz frequency range, overlapping with the ALMA B3 scans (see Fig. 3). In this frequency range, we expected the lower J CO(5-4) and CO(7-6) transitions for the $z = 6.12$ and 8.5 solutions, respectively. In this case, the non-detection disfavors the higher- z solutions. We detect the 97 GHz line, further confirming the ALMA detection and the spectroscopic redshift of $z_{\text{spec}} = 3.7515$.

With $z_{\text{spec}} = 3.75$ confirmed, the 97.03 and 145.5 GHz lines correspond to CO(4-3) and CO(6-5), respectively. For CO(4-3), the measured line flux is consistent between the two instruments. To characterise the velocity-integrated flux density, and given the non-Gaussian shape of the line profiles, we calculated the full line-width at zero intensity (FWZI). Specifically, we measured an integrated line flux in the sky-plane (lensing-uncorrected) of 5.7 ± 1.0 and 4.0 ± 0.3 Jy km s⁻¹ for ALMA and LMT, respectively, over ~550 km s⁻¹. For the higher J transition CO(6-5), we obtain an integrated flux of 6.6 ± 1.1 Jy km s⁻¹. We also find two low S/N (i.e. $4 > \text{S/N} > 2$; see Fig. B.1) tentative detections at

¹ <https://www.iram.fr/IRAMFR/GILDAS/>

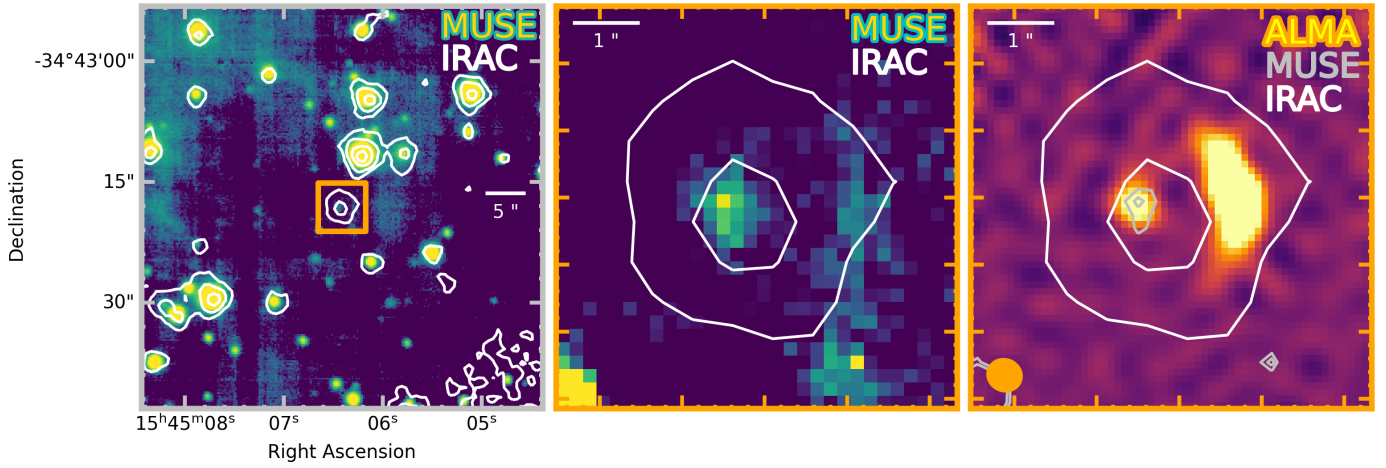


Fig. 2. *Left panel:* Multi Unit Spectroscopic Explorer (MUSE) white-light (4750–9350 Å) median stack image of a $50 \times 50''$ region centred on the lens coordinates, with the orange square representing a $3 \times 3''$ region. The 1, 2, 5, and 10 σ Infrared Array Camera (IRAC) contours are shown in white. *Central panel:* $6 \times 6''$ MUSE zoom-in with the 1 and 2 σ IRAC white contours overlaid. Both IRAC and MUSE images are aligned using *Gaia*-DR3 stars within a $30''$ radius circle around the source. The faint linear emission feature does not overlap with the ALMA main arc, but instead corresponds to the noise arising from the ‘gaps’ between the MUSE detectors. *Right panel:* Same as the central panel, but overlaid on the ALMA Band 7 image of the background galaxy at $0.75''$ resolution (robust = 1). The IRAC and MUSE 1 and 2 σ contours are shown in white and grey, respectively, to illustrate the relative position of the lens with respect to the background galaxy in the image plane.

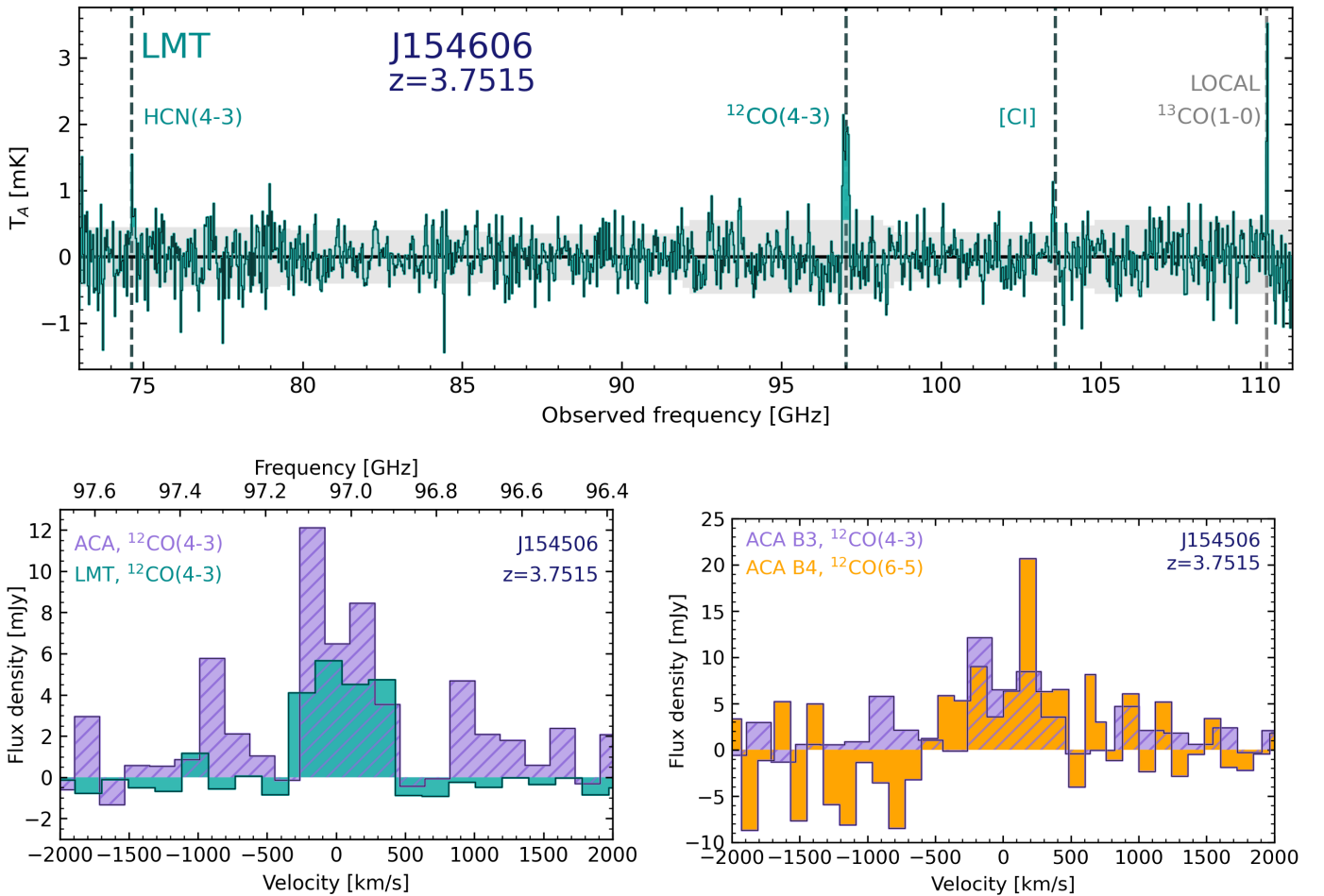


Fig. 3. *Top panel:* Large Millimetre Telescope (LMT) spectrum of J154506 obtained with the Redshift Search Receiver (RSR) instrument. Transitions with $S/N > 3$ compatible with either the J154506 redshift or the local molecular clouds are marked with vertical dashed lines and labelled in teal and grey, respectively. *Bottom:* Velocity comparison of the continuum-subtracted line profile for the $^{12}\text{CO}(4-3)$ line detected with ACA and LMT, respectively (*left*), and $^{12}\text{CO}(4-3)$ versus $^{12}\text{CO}(6-5)$ transitions from ALMA/ACA (*right*). The LMT spectrum in the bottom panel is binned to two-channel width to match the velocity resolution of the compared lines.

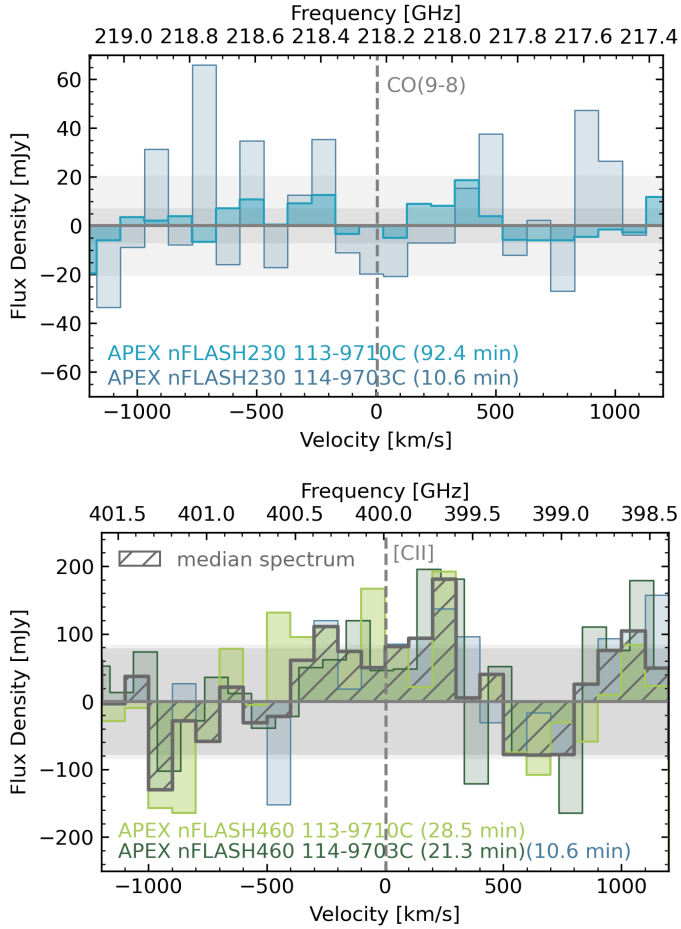


Fig. 4. Spectra from APEX nFLASH230 (*top panel*) and nFLASH460 (*bottom panel*), centred at the redshifted ($z = 3.7515$) frequencies of the CO(9-8) and [CII] emission lines, respectively. The independent runs are colour-coded and labelled accordingly. The derived RMS (1σ noise level) is indicated by light grey shading, while dark grey arises from the overlap region of the errors from distinct datasets. The CO(9-8) line is not detected, but [CII] is detected at >2 sigma in all three scans. For [CII], the median-averaged spectrum ($S/N > 4$) is shown in dark grey, with the area shaded using diagonal grey hatching.

74.6 and 103.6 GHz, consistent with HCN ($J = 4-3$) and [C 13 P $_1$ - 3 P $_0$] at that redshift.

We also find two $S/N \sim 3$ detections corresponding to $\text{H}_2\text{O}^+(2_{02} - 1_{11})_{(3/2-1/2)}$ and $\text{H}_2\text{O}^+(2_{11} - 2_{02})_{(3/2-3/2)}$ at 151.9 and 161.3 GHz, respectively. Although these specific transitions have not previously been detected in local ultraluminous IR galaxies (e.g. van der Werf et al. 2010; Rangwala et al. 2011) or in high redshift SMGs (Reuter et al. 2023), the detection of similar rotational transitions at $z = 2-4$ (Yang et al. 2016, 2019) provides compelling support for our detections. Finally, a very narrow spike is observed at 110 GHz, which most likely corresponds to foreground $^{13}\text{CO}(1-0)$ emission (i.e. from the Milky Way in the direction of J154506).

Observations with APEX covered the CO(9-8) and [CII] lines at $z = 3.75$. Although the project was not completed and CO(9-8) is not detected, we find an $S/N > 4$ detection at 400 GHz corresponding to [CII] at $z = 3.75$. Figure 4 shows the apparent flux density centred at the redshifted frequency of the CO(9-8) (218.23 GHz) and [CII] (399.99 GHz) emission lines at $\approx 100 \text{ km s}^{-1}$ resolution. We did not detect any CO(9-8) emission in the APEX spectra, even at 7 mJy rms. However,

Table 1. Integrated line fluxes before magnification correction.

Line	Telescope/ Instrument	Line width km s^{-1}	Flux density Jy km s^{-1}
$^{12}\text{CO}(9-8)^a$	APEX/nFLASH	550	2.1 ± 4.3
$^{12}\text{CO}(9-8)^b$	ALMA	550	2.0 ± 1.5
$^{12}\text{CO}(6-5)$	ALMA/ACA	603 ± 60	6.6 ± 1.1
$^{12}\text{CO}(4-3)$	ALMA/ACA	543 ± 90	5.7 ± 1.0
$^{12}\text{CO}(4-3)$	LMT/RSR	580 ± 97	4.0 ± 0.5
$^{12}\text{CO}(4-3)^c$	NRO	625 ± 120	6.5 ± 0.7
$^{12}\text{CO}(2-1)^c$	ATCA	543 ± 106	3.0 ± 0.5
[CI]	LMT/RSR	362 ± 135	1.0 ± 0.3
[CI]	ALMA/ACA	340 ± 113	2.9 ± 1.0
[CII] ^d	APEX/nFLASH	598 ± 85	71.5 ± 15.4
$\text{H}_2\text{O}^+(2_{02} - 1_{11})_{(3/2-1/2)}$	ALMA/ACA	230 ± 116	4.3 ± 1.0
$\text{H}_2\text{O}^+(2_{11} - 2_{02})_{(3/2-3/2)}$	ALMA/ACA	548 ± 110	7.5 ± 1.6
HCN(4-3)	LMT/RSR	502 ± 126	1.0 ± 0.3

Notes. ^aValue obtained by forcing a measurement in the spectra, assuming a line velocity of 550 km s^{-1} . ^bFlux derived from ALMA spectra in which only half of the line is covered. A conservative 75% error is assigned to the value. ^cMeasurements from Tamura et al. (2025). ^dThe provided flux corresponds to the median spectrum; the measurements for the three independent spectra are consistent within the errors.

to constrain the CO Spectral Line Energy Distribution (SLED), see Section 6.2), we performed a forced measurement by integrating the spectrum over a velocity width of 550 km s^{-1} (see Table 1). Similarly, for the ALMA CO(9-8) spectrum presented in Tamura et al. (2025), where only approximately half of the line profile is covered and no measurements are provided, we estimated the total flux by scaling the integrated observed spectrum to an assumed line width of 550 km s^{-1} . Due to the inherent uncertainty of such an estimate, we assign a conservative 75% error to this value. The APEX non-detection is consistent with this estimate, as its significantly higher rms is more than three times the ALMA measured flux density. The three independent [CII] observations are shown in the lower panel of Fig. 4. Despite their diverse integration times, a very similar sensitivity (i.e. $\approx 80 \text{ mJy}$) was achieved in all cases. Although each independent spectrum provides only a $S/N = 2-3$ [CII] detection, the consistency between the three runs, along with the very similar widths (see Fig. 4) and spectral shape resembling that of CO(6-5), allow us to confirm the presence of [CII] emission. Additionally, the median spectrum yields an $S/N > 4$ detection.

Our spectroscopic redshift of $z_{\text{spec}} = 3.7515 \pm 0.0005$ is in excellent agreement with the redshift recently reported by Tamura et al. (2025) ($z = 3.753 \pm 0.001$). Furthermore, our independent ALMA detection of the CO(4-3) transition at 97 GHz yields an integrated line flux of $5.7 \pm 1.0 \text{ Jy km s}^{-1}$, consistent within uncertainties, with their measurement ($6.5 \pm 0.7 \text{ Jy km s}^{-1}$). This agreement strengthens the robustness of our flux measurements and derived properties (see Sections 6.1 and 6.2). The lower RSR/LMT fluxes ($4.0 \pm 0.3 \text{ Jy km s}^{-1}$ for CO(4-3)) could be influenced by known instrumental systematic calibration biases².

The observed extreme $S_{250\mu\text{m}}/S_{500\mu\text{m}}$ flux ratio (see Figure 1) and the photometric redshift of J154506 initially suggested a potentially higher-redshift system. However, our spectroscopic redshift of $z_{\text{spec}} = 3.7515$, combined with a relatively cold dust temperature ($T = 38 \text{ K}$; see also Section 6) reveals a less extreme,

² LMT-SCI-MAN-002, Version v2.0

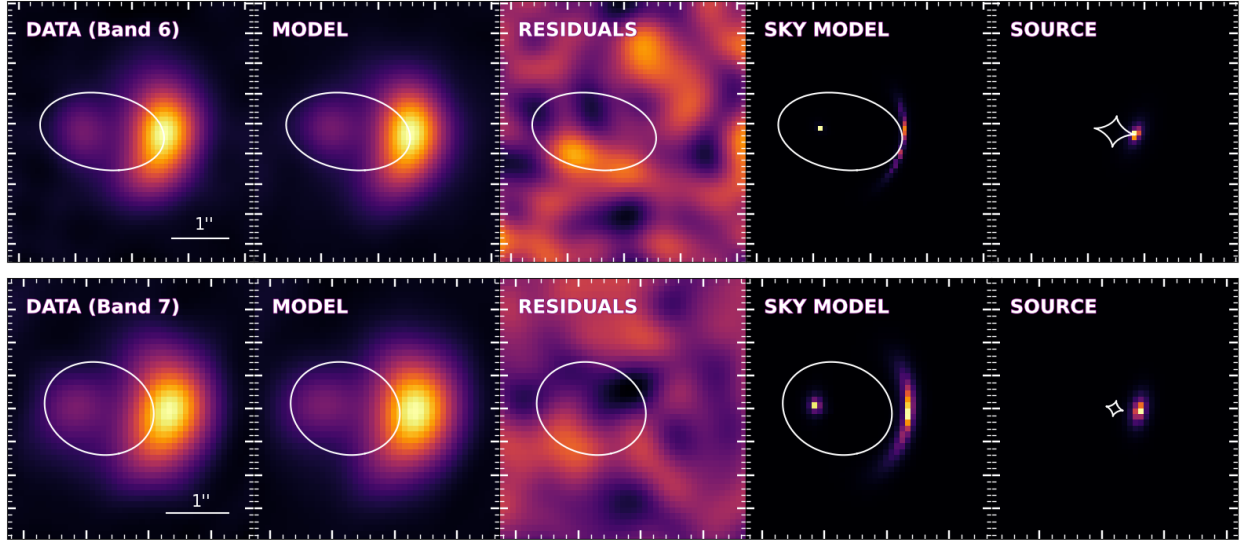


Fig. 5. Results from the lens modelling analysis in the uv -plane for B6 (*top*) and B7 (*bottom*). From left to right: the panels show the ‘dirty’ data image, ‘dirty’ model image, ‘dirty’ residuals, sky model (i.e. deconvolved), and source model. The white line represents the critical curve (first four panels) and the caustic curve (rightmost panel).

though still high-redshift system. This highlights the inherent degeneracy between dust temperature and redshift in broadband colour photometric redshift indicators (e.g. Chapman et al. 2004; Casey et al. 2014; Dowell et al. 2014), emphasising the need for spectroscopic confirmation and comprehensive FIR fitting to characterise dusty star-forming galaxies (DSFGs). Analysis of the UV-to-Radio SED often provides more accurate photometric redshifts and physical properties. However, for J154506, foreground contamination combined with the large uncertainty in the Galactic extinction caused by the Lupus-I molecular cloud (see Rygl et al. 2013), makes it challenging to constrain the background source stellar emission. The foreground is difficult to model without high-resolution, long-integration optical-to-MIR data, whereas the Lupus-I extinction differentially impacts the SED, causing significant absorption at shorter (UV-to-NIR) wavelengths, where it combines with intrinsic galaxy dust extinction. These factors render a unified rest-frame UV-to-FIR energy-balanced SED fitting unfeasible and makes SED-derived properties, such as the stellar mass, highly uncertain.

5. Lens modelling and magnification

Deriving the intrinsic physical properties of J154506 requires both a magnification factor and a confirmed redshift. To determine the magnification factor, we constructed a mass model for the lens and a light model for the source that best fit our observations. Because the spectroscopic redshift of the foreground lens could not be constrained, our modelling primarily relied on reproducing the observed image geometry, which is less sensitive to the exact lens redshift. The magnification factor, which is primarily dependent on the image geometry, remains largely unaffected by the unconstrained lens redshift. For this analysis, we used the publicly available software PYAUTOLENS (Nightingale & Dye 2015; Nightingale et al. 2018) and conducted the analysis directly in the uv -plane (e.g. Dye et al. 2018; Maresca et al. 2022). This uv -plane modelling approach consistently outperforms sky-plane modelling for simulated ALMA observations by avoiding biases and spurious structures introduced by the CLEAN process (Maresca & Dye 2025). We mod-

elled the lens as a spherical isothermal ellipsoid (SIE) and the source as a Sérsic profile (Sérsic 1963). The model parameters were optimised by fitting only the continuum emission in B6 and B7 independently, using the non-linear sampler Dynesty. Note that for B6, we used only spectral windows 0 and 1 due to the presence of emission lines in the other spectral windows. The lens centre was left as a free parameter, with a Gaussian prior centred between the two multiple images and a standard deviation of $1''$. The lens position recovered by the parametric model is consistent with the centroid of the MUSE detection. The median positional offset ($0.1''$) is better than the MUSE spatial sampling ($0.2''/\text{pixel}$). The best-fit lens mass model parameters are $R_E = 0.86 \pm 0.01$, $q = 0.58 \pm 0.02$, and $\theta = -8 \pm 2$, in B6, and $R_E = 0.78 \pm 0.01$, $q = 0.81 \pm 0.03$, and $\theta = -10 \pm 7$, in B7. Here, R_E is the Einstein radius (arcsec), q is the axis ratio defined as the ratio of the minor axis to the major axis ($q = b/a$), and θ is the position angle (in degrees) of the major axis measured counterclockwise from the positive x axis in the image plane coordinates. The derived background-source parameters for B7 are an effective radius of $R_{\text{eff}, B7} = 0.147^{+0.009}_{-0.008}$ arcsec and a source centroid position relative to the lens centre of $(x, y)_{B7} = (0.56 \pm 0.01, -0.07 \pm 0.01)$ arcsec. For B6, we find an effective radius of $R_{\text{eff}, B6} = 0.22^{+0.12}_{-0.04}$ arcsec and a source centroid position of $(x, y)_{B6} = (0.49 \pm 0.01, -0.01 \pm 0.02)$ arcsec. The larger and more asymmetric uncertainty in $R_{\text{eff}, B6}$ reflects the slightly lower S/N relative to B7. Figure 5 presents the results of the modelling analysis. Given the low resolution of our data, the simple parametric models used for the lens and source are sufficient to fit the observations down to the noise level. However, a subtle correlation between the residual images in B6 and B7 suggests that the model may not fully capture the intricate structure of the source or could hint at unmodelled substructure within the foreground lensing object. We derive magnification factors of $\mu = 7.4 \pm 0.6$ and $\mu = 4.5 \pm 0.4$ for B6 and B7, respectively. For the remainder of this paper, we adopt the average magnification $\mu = 6.0 \pm 0.4$ to derive intrinsic properties. Our derived magnification factors agree with those recently reported ($\mu = 6.6$; Tamura et al. 2025) from a simple model in the image plane assuming $z_{\text{lens}} = 0.5$.

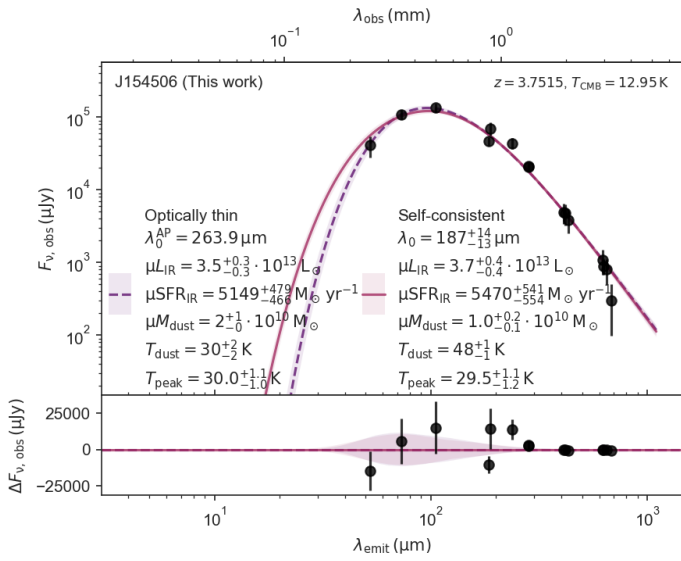


Fig. 6. Far-infrared SED of J154506 fitted using MERCURIUS. The black circles indicate the dust continuum detections. The dashed line shows the best-fit model assuming optically thin emission. The main derived physical properties, before magnification correction, are also shown. The corner plot and magnification-corrected values are provided in Appendix F.

6. Properties of the cold interstellar medium

In this section, we derive the initial estimates of the cold interstellar medium properties by modelling the measured dust photometry and velocity-integrated line flux densities. First, we analyse the well-sampled FIR SED of J154506 to characterise its dust continuum emission and derive global FIR properties. Next, we present the results of our combined dust and line modelling using the TURBULENT Non-Equilibrium Radiative transfer (TUNER) framework (See Section 6.2 and Appendix E). Finally, we discuss [CII]-derived properties and the potential contribution of an AGN.

6.1. Dust emission and FIR-derived properties

We first fitted J154506 using the Bayesian FIR SED PYMULTINEST fitting code MERCURIUS (Multimodal Estimation Routine for the Cosmological Unravelling of Rest-frame Infrared Uniformised Spectra; Witstok et al. 2022), which employs a nested sampling algorithm (PYMULTINEST, Buchner et al. 2014) to fit a greybody spectrum to FIR photometry. MERCURIUS explicitly accounts for the cosmic microwave background (CMB) following the approach of da Cunha et al. (2013). For fitting, we considered rest-frame FIR wavelengths from 10 to $10^3 \mu\text{m}$. First, we assumed an entirely optically thin scenario for dust emission, and left the dust temperature (T_{dust}) and emissivity index (β_{dust}) free to vary. We then used a more physically realistic, self-consistent dust opacity model that accounts for wavelength dependence and the transition between optically thin and thick regimes, parametrised following Witstok et al. (2022). We set our T_{dust} priors by disfavouring extremely high dust temperatures, consistent with recent studies (e.g. Witstok et al. 2022, 2023; Valentino et al. 2024). Specifically, we used a default gamma distribution with a shape parameter ($a = 1.5$), and for β_{dust} , we imposed a Gaussian prior centred at 1.8 with a standard deviation of 0.25. Following Schouws et al. (2022), we adopted

a dust emissivity coefficient (κ) of the form $\kappa(\nu) = \kappa(\nu/\nu_0)^\beta$, with $\kappa = 8.94 \text{ cm}^2 \text{ g}^{-1}$ at $\lambda_{\text{ref}} = 158 \mu\text{m}$ (Hirashita et al. 2014). This value of κ is appropriate for dust grains ejected by supernovae (SNe) after reverse shock destruction (Hirashita et al. 2014).

Figure 6 presents the best fit of a modified blackbody for J154506. Briefly, we obtain an emissivity indices of $\beta_{\text{dust}} = 2.0 \pm 0.1$ and 2.1 ± 0.1 , and dust temperatures of 30 ± 2 and 48 ± 1 K for the optically-thin and self-consistent scenarios, respectively. The derived intrinsic IR luminosity is $L_{\text{IR}} = 6\text{--}7 \times 10^{12} L_\odot$, and the IR-based SFR ranges from 860 ± 80 to $910 \pm 90 M_\odot \text{ yr}^{-1}$. Additionally, after correcting for magnification, we derive dust masses of $3.4 \pm 1.6 \times 10^9 M_\odot$ and $1.7 \pm 0.3 \times 10^9 M_\odot$ for the optically-thin and variable dust optical depth models, respectively.

The most robust quantities in our analysis are the integrated IR luminosities (L_{IR} and L_{FIR}) and the approximate peak of the dust SED, which are very well constrained by all available integrated flux measurements across the dust SED. While this approach provides a useful first-order characterisation, several parameter degeneracies are inherent to such simplified, integrated modelling. Dust mass estimates are highly dependent on the assumed κ value and optical depth, which can vary with grain composition and processing history. For example, if J154506 has a dominant contribution from dust grown in the ISM (e.g. graphite and silicate grains) with higher κ , this could lead to an overestimation of the inferred dust mass. The fitted T_{dust} can also degenerate with λ_0 (λ at which the optical depth equals unity), β , and the assumed optical depth regime. In particular, adopting an optically thin assumption—where radiation from a central source passes through dust without significant absorption or re-emission—is likely unrealistic for a highly dust-obscured system such as J154506, as many high-redshift starbursts show substantial FIR optical depths (e.g. Jin et al. 2022). Nevertheless, even the self-consistent model employed here contains simplifying assumptions, including neglecting multiple dust components, temperature distributions along the line of sight, and interactions with the surrounding gas. The variation in dust temperature predictions across models underscores the limitations of oversimplified radiative transfer approaches and the need for a more sophisticated modelling (see Section 6.2).

6.2. Radiative transfer model results

We employed the state-of-the-art TUNERmodel to simultaneously fit the dust and CO line SEDs and to derive the molecular gas excitation properties. The TUNER model is described in detail by Harrington et al. (2021), and we refer the reader to that work for a comprehensive overview (see also Strandet et al. 2017; Jarugula et al. 2021). Briefly, these non-local thermodynamic equilibrium (non-LTE) radiative transfer calculations model the CO line intensities and dust continuum using a large velocity gradient approximation (LVG; see, e.g. Goldreich & Kwan 1974) and a lognormal probability distribution function to describe the gas volume density (see Krumholz et al. 2005). For this initial combined line and continuum SED analysis, we followed Harrington et al. (2021) and fixed some of the unknown parameters. Specifically, we fixed the $[\text{CO}]/[\text{H}_2]$ gas-phase abundance to a fiducial Milky Way value (i.e. $\log([\text{CO}]/[\text{H}_2]) = -4.0$). The initial model fits, obtained with a free molecular gas-to-dust mass ratio (GDMR), yielded a median GDMR of 100, which we subsequently fixed to reduce degeneracy in the parameter space. Additional details are described in Appendix E. We note that in this modelling we

explicitly assumed the same value of $\kappa = 8.94 \text{ cm}^2 \text{ g}^{-1}$ at $158 \mu\text{m}$ as used in the MERCURIUS modelling above.

Figure 7 presents the best-fit model along with the 16th–84th percentile ranges for the observed CO line and dust SEDs. The lognormal distribution derived from the best-fit mean density is sampled by 50 bins spanning densities of $10\text{--}10^7 \text{ cm}^{-3}$, as shown in Figure 7. The dust SED peak and turnover are well-sampled, with dominant contributions from more diffuse molecular gas in the $10^{2\text{--}4} \text{ cm}^{-3}$ range. This suggests that most of the FIR emission originates from this relatively diffuse to moderately dense molecular medium, rather than from highly compact star-forming regions that may be more common in extreme starbursts or AGN-dominated systems (Narayanan & Krumholz 2014; Scoville et al. 2017; Harrington et al. 2021). The CO line SED peaks near the CO(5-4) transition, exhibiting a sharp turnover that contrasts with the flatter high-J CO SLEDs of quasi-stellar objects (QSOs) and the most extreme starbursts (e.g. Rosenberg et al. 2015; Harrington et al. 2021). Overall, CO line excitation is dominated by slightly denser molecular gas of $10^{3\text{--}4} \text{ cm}^{-3}$, which is typical of main-sequence DSFGs and moderate starbursts at high redshift (Daddi et al. 2015; Valentino et al. 2020; Liu et al. 2021).

The derived dust properties are consistent with the Ultra-Luminous InfraRed Galaxy (ULIRG) nature of this object, with a 16th–84th percentile range of $L_{\text{IR}}(8 - 1000 \mu\text{m}) = 5.5 - 6.5 \times 10^{12} L_{\odot}$ after correcting for magnification, consistent with the MERCURIUS fits. The well-constrained TUNER model fits the observed data comparably to the best-fit MERCURIUS model, yielding a dust emissivity index of 2.2 and a relatively cold dust temperature of 38 K. This finding supports the prevalence of cold dust in high-redshift starbursts as a natural consequence of deeply embedded SF within gas- and dust-rich environments (e.g. Scoville et al. 2023), a phenomenon first predicted by early dust SED models for young stars (e.g. Scoville & Kwan 1976).

Understanding the coupling between gas and dust in galaxies provides crucial insights into the dominant heating mechanisms and overall physical conditions of their ISM. A key diagnostic for this coupling is the ratio of the gas kinetic temperature (T_{k}) to the dust temperature (T_{d}), since distinct heating processes affect these components differently. Although J154506 has a strong intrinsic far-IR luminosity, the median gas-to-dust temperature ratio is $T_{\text{k}}/T_{\text{d}} = 1.1 \pm 0.2$. The median derived value for similarly bright $z = 1\text{--}3.5$ *Planck*-selected starbursts is $T_{\text{k}}/T_{\text{d}} = 2\text{--}3$ (Harrington et al. 2021). This ratio has been proposed as a proxy for mechanical versus photoelectric heating contributions (Harrington et al. 2021; Dunne et al. 2022) that may be responsible for molecular gas heating. The near-unity value for J154506 is considerably lower, suggesting that mechanical heating is not a dominant powering mechanism. As discussed by Harrington et al. (2021), this value approaches unity when the gas and dust temperatures are coupled, typically at mean densities above $10^{4\text{--}5} \text{ cm}^{-3}$. The 10^4 cm^{-3} CO-emitting gas dominates both the observed CO line SED and the molecular gas mass in this system.

The model fit parameters enable the calculation of the total intrinsic molecular gas mass, $M_{\text{ISM}} = 3.1 - 8.5 \times 10^{11} M_{\odot}$, CO luminosity $L'_{\text{CO}(1-0)} = 4.1 - 6.5 \times 10^{10} \text{ K km s}^{-1} \text{ pc}^2$, and the mass-to-light conversion factor $\alpha_{\text{CO}(1-0)} = 5.2 - 17 M_{\odot} \text{ pc}^{-2} (\text{K km s}^{-1})^{-1}$ corresponding to the 16–84th percentile ranges. The spatially unresolved measurements, combined with a fixed GDMR, and [CO]/[H₂] values used in this initial modelling, prevent a more tightly constrained molecular gas mass. Nevertheless, the derived conversion factor is sig-

nificantly higher than the commonly assumed ULIRG value of $0.8 M_{\odot} \text{ pc}^{-2} (\text{K km s}^{-1})^{-1}$ (Downes & Solomon 1998), despite the total IR luminosity of J154506 exceeding $10^{12} L_{\odot}$.

Despite providing only a global view of J154506’s molecular gas and dust properties, our analysis yields reliable ISM properties. This confidence stems from the extensive coverage of the source’s dust emission and thorough sampling of its CO ladder. These data, combined with the narrowness of the marginalised posterior distributions of the parameters (see Appendix F), reinforce the robustness of this initial characterisation, even if a more comprehensive analysis remains beyond the scope of the present study. While future spatially resolved studies of the dust and cold gas will allow for more precise estimates, our initial findings indicate that this submm-selected lensed object exhibits less extreme molecular gas excitation conditions compared to other known high-redshift DSFG and QSO systems. Moreover, its substantial molecular gas reservoir suggests the potential to evolve into a hyperluminous infrared galaxy (HyLIRG) at cosmic noon ($z = 2\text{--}3$) upon reaching the peak of its starburst activity.

6.3. [CII] as a tracer of cold ISM

The [CII] $158 \mu\text{m}$ line is the brightest FIR line and the dominant coolant of neutral and ionised gas. It originates primarily in photo-dissociation regions (PDRs), where far-ultraviolet photons from young massive stars interact with molecular clouds, but it can also arise from the diffuse ionised medium and cold neutral medium (e.g. Lagache et al. 2018). Since our observations are spatially unresolved and have a modest S/N (<5), our analysis derives global constraints based on the ability of [CII] to probe gas content and trace SF activity (i.e. Carilli & Walter 2013) up to very high redshift (e.g. Capak et al. 2015; Bouwens et al. 2022).

We derive an observed [CII] luminosity of $3.2 \times 10^{10} L_{\odot}$ ($L'_{\text{[CII]}} = 14.9 \times 10^{10} \text{ K km s}^{-1} \text{ pc}^2$), corresponding to an intrinsic $L_{\text{[CII]}}$ of $5.4 \times 10^9 L_{\odot}$. This corresponds to an $L_{\text{[CII]}}$ to L_{FIR} ratio of 8.3 to 9.9×10^{-4} , depending on the L_{FIR} adopted (see Sections 6.1 and 6.2). This ratio is comparable to values ($L_{\text{[CII]}}/L_{\text{FIR}} = 3.6\text{--}25.7 \times 10^{-4}$) reported by Gullberg et al. (2015) for 20 SPT galaxies at $z = 2.1\text{--}5.7$ with [CII] luminosities of $1.4 - 9.2 \times 10^{10} L_{\odot}$.

Using the high-redshift relations from De Looze et al. (2014), we derive an SFR of $840 M_{\odot} \text{ yr}^{-1}$. This [CII]-derived SFR is remarkably consistent with that obtained from the median total infrared luminosity ($L_{\text{TIR}} \sim 6 \times 10^{12} L_{\odot}$). This finding is noteworthy, as studies of infrared-luminous galaxies ($L_{\text{IR}} > 10^{12}$) galaxies commonly report a suppression of [CII] emission relative to infrared emission, known as the ‘[CII] deficit’ (e.g. Díaz-Santos et al. 2013; Lutz et al. 2016; Herrera-Camus et al. 2018). For J154506, this suggests that the [CII] emission serves as an efficient cooling channel, suggesting that physical conditions (e.g. radiation field intensity and gas density) do not substantially suppress [CII] emission. This behaviour aligns with observations of other high-redshift sources, where [CII] effectively traces SF (e.g. Carniani et al. 2020; Schaerer et al. 2020).

6.4. Possible AGN contribution

The intrinsic IR-based SFR of J154506 is remarkably high, estimated at $\geq 840 M_{\odot} \text{ yr}^{-1}$, approaching the limits of typical maximal starburst systems (i.e. Casey et al. 2014; Béthermin et al. 2015; Tacconi et al. 2020). This raises the possibility that the

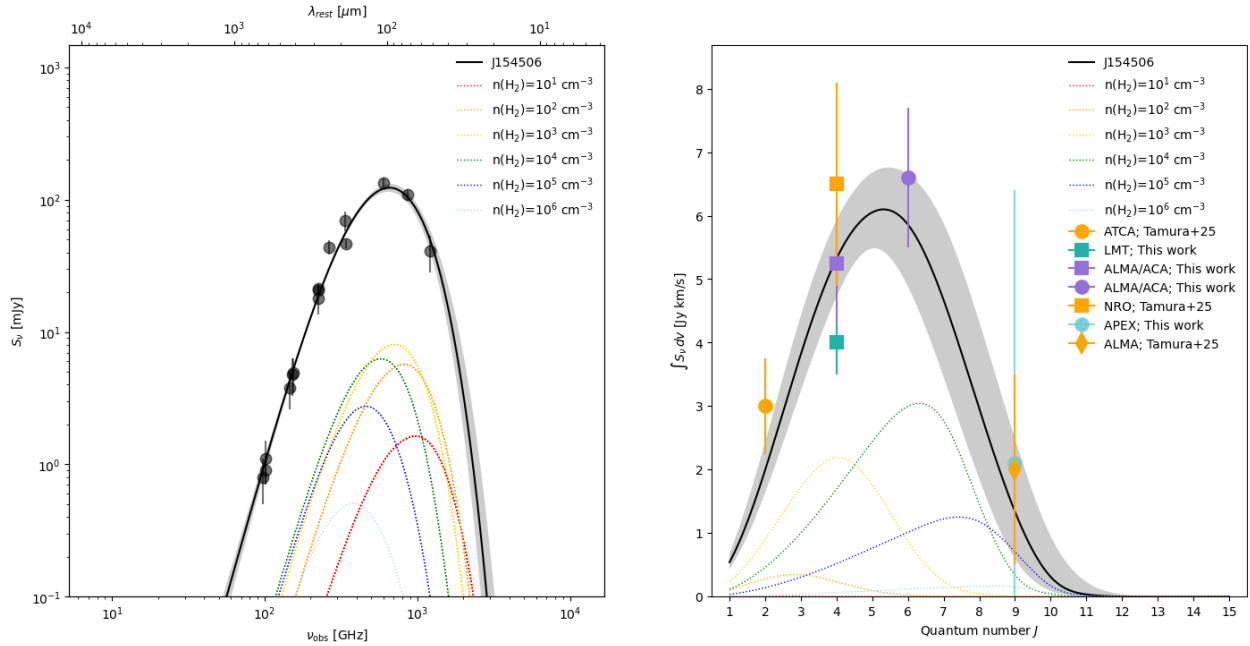


Fig. 7. Results from the TUNER model for the observed dust SED and velocity-integrated CO line flux densities. The 50th percentile is shown by a dashed black line and the 16–84th percentile range is shown as a grey shaded area. The different dashed, colour-coded curves denote the representative contributions to the observed line and continuum SEDs from gas at specific molecular gas densities. We sampled the density grid using 50 bins, but we only plot a subset of representative density components (coloured lines) to highlight their relative contribution. These densities correspond to $\log(n(\text{H}_2)) = 1$ (red), 2 (orange), 3 (yellow), 4 (green), 5 (dark blue), and 6 (light blue) cm^{-3} , as determined by sampling the lognormal probability distribution function of the mean H_2 density. For the CO SED (right panel), contributions are scaled up by a factor of five for visibility. All observed data are shown as colour-coded symbols.

total infrared luminosity, and consequently the derived SFR, might be contaminated by emission from a dust-obscured AGN. The AGN fraction (f_{AGN}) can, however, be constrained using the upper limit on the Multiband Imaging Photometer for Spitzer (MIPS) $24\ \mu\text{m}$ flux, which probes the rest-frame $\sim 5\ \mu\text{m}$ emission at $z = 3.75$. For this analysis, we assume that foreground extinction from the Lupus-I molecular cloud at $24\ \mu\text{m}$ is negligible. For J154506, the ratio $\nu L_\nu(5\ \mu\text{m})/L_{\text{IR}} < 0.04$, suggesting that the source is SF-dominated, as this value is well below the threshold of 0.1 typically indicative of a significant AGN contribution (Hernán-Caballero et al. 2009).

This aligns with the near-unity $T_{\text{k}}/T_{\text{d}} \approx 1.1$, suggesting that ISM heating is largely dominated by star formation rather than AGN activity. In AGN-dominated systems, strong X-ray and UV radiation from the central source influence the ISM through cosmic ray heating, ionisation, and turbulence. This can significantly enhance T_{k} while leaving the dust temperature relatively low, leading to $T_{\text{k}}/T_{\text{d}} \gg 1$ (e.g. Schleicher et al. 2010; Papadopoulos 2010; Narayanan & Krumholz 2014). Observational studies confirm that AGN hosts and starburst-dominated HyLIRGs typically exhibit $T_{\text{k}}/T_{\text{d}} > 2$ (e.g. Harrington et al. 2021), whereas moderate star-forming systems tend to maintain lower ratios of $T_{\text{k}}/T_{\text{d}} = 1\text{--}1.5$ (e.g. Daddi et al. 2015; Valentino et al. 2020). In addition, the CO line SED indicates that the molecular gas excitation in this system is not driven by AGN-related X-ray heating or intense mechanical shocks, which typically produce enhanced high- J CO emission. However, we acknowledge that a minor AGN contribution cannot be definitively ruled out. Deeper observations are required to more stringently constrain the high- J emission. Current samples with well-mapped CO SLEDs remain heavily biased towards low-redshift galaxies, lower- J transitions, and extreme systems, limiting direct comparisons with high-redshift DSFGs.

7. Summary and conclusions

We confirm the extragalactic and strongly lensed nature of J154506, an extremely submm-bright and enigmatic source that was initially thought to be a (sub)stellar object due to its location towards the Lupus-I molecular cloud. By combining archival data with new submm spectral scans, we spectroscopically confirm its redshift and characterise the gas, dust, and physical properties of J154506, yielding the following key results:

- Using ALMA/ACA and LMT/RSR, we detect two significant ($S/N > 5$) broad ($\sim 600\ \text{km s}^{-1}$) emission lines at 97.0 and 145.5 GHz, corresponding to CO(4-3) and CO(6-5), respectively. These detections yield a spectroscopic redshift of $z_{\text{spec}} = 3.7515 \pm 0.0005$ and confirm J154506 as an extragalactic source, consistent with the arc-shaped structure in ALMA continuum images.
- We also detect several lower S/N ($= 2\text{--}3$) lines: [CI], HCN(4-3), and two H_2O^+ transitions ($\text{H}_2\text{O}^+(2_{02} - 1_{11})_{(3/2-1/2)}$ and $\text{H}_2\text{O}^+(2_{11} - 2_{02})_{(3/2-3/2)}$), along with additional tentative detections.
- We performed gravitational lens modelling using PYAULLEN, fitting the ALMA B6 and B7 continuum data directly in the uv -plane with a singular isothermal ellipsoid (SIE) lens model and a Sérsic source profile, yielding an average magnification factor of $\mu = 6.0 \pm 0.4$. Although observing conditions prevented a spectroscopic redshift confirmation of the foreground lens with MUSE and FORS2, these optical observations were crucial for accurately pinpointing its position.
- We detect the [CII] $158\ \mu\text{m}$ fine-structure line at 400 GHz using APEX/nFLASH in three independent spectra. From the median spectrum, we derive an intrinsic luminosity of

$5.4 \times 10^9 L_{\odot}$ after correcting for magnification, and an SFR of $\sim 840 M_{\odot} \text{ yr}^{-1}$.

- The simple modified blackbody fit to the FIR photometry of J154506 yields a relatively cold dust temperature (30–48 K), an emissivity index β of 2.0, and a dust mass of $4.5 \times 10^9 M_{\odot}$.
- The combined modelling of the dust SED and CO excitation ladder constrains the dust temperature to 38 K and suggests that the FIR emission arises primarily from moderately dense rather than compact, high-pressure environments typical of extreme starbursts or AGNs. Additionally, we find that the CO excitation ladder peaks near CO(5-4) and is dominated by a slightly denser molecular gas. Its sharp turnover further supports the interpretation that J154506 is a highly star-forming galaxy, but not a QSO or an extreme system. The derived near-unity kinetic-to-dust temperature ratio suggests a minor AGN contribution for J154506.

Our results highlight the importance of mapping even low Galactic latitudes when searching for such extreme and scarce sources and demonstrate their potential to probe the ISM properties of high-redshift galaxies in unprecedented detail. A spectroscopic confirmation of the foreground is required to further characterise this extreme system.

Acknowledgements. We thank the anonymous referee for a thoughtful and detailed review, which has significantly improved the clarity and quality of this manuscript. This paper makes use of the following ALMA data: ADS/JAO.ALMA#2015.1.00512.S; ADS/JAO.ALMA#2017.1.00303.S; ADS/JAO.ALMA#2018.1.00126.S; ADS/JAO.ALMA#2019.1.00245.S; ADS/JAO.ALMA#2021.2.00097.S; ADS/JAO.ALMA#2023.1.00251.S. ALMA is a partnership of ESO (representing its member states), NSF (USA) and NINS (Japan), together with NRC (Canada), MOST and ASIAA (Taiwan), and KASI (Republic of Korea), in cooperation with the Republic of Chile. The Joint ALMA Observatory is operated by ESO, AUI/NRAO, and NAOJ. M.A. is supported by FONDECYT grant number 1252054, and gratefully acknowledges support from ANID Basal Project FB210003 and ANID MILENIO NCN2024_112. A.S.M. acknowledges support from ANID/Fondo 2022 ALMA/31220025. E.F.-J.A. acknowledges support from UNAM-PAPIIT projects IA102023 and IA104725, and from CONAHCYT Ciencia de Frontera project ID: CF-2023-1-506. MIR acknowledges the support of the Spanish Ministry of Science, Innovation and Universities through the project PID-2021-122544NB-C43. M.S. was financially supported by Becas-ANID scholarship #21221511, and also acknowledges support from ANID BASAL project FB210003. This work would not have been possible without the long-term financial support from the Mexican Humanities, Science and Technology Funding Agency, CONAHCYT (Consejo Nacional de Humanidades, Ciencias y Tecnologías), and the US National Science Foundation (NSF), as well as the Instituto Nacional de Astrofísica, Óptica y Electrónica (INAOE) and the University of Massachusetts, Amherst (UMass). The operation of the LMT is currently funded by CONAHCYT grant #297324 and NSF grant #2034318. The data described in this paper include LMT observations conducted under the scientific program 2024-S1-MX-11. The authors acknowledge the scientific and technical support of the LMT staff during the observations and generation of data products provided to the authors. *Software:* In addition to the software mentioned in the main text, this work also employed Astropy, a community-developed core Python package for Astronomy (Astropy Collaboration 2013, 2022); Matplotlib (Hunter 2007); Numpy; SciPy (Virtanen et al. 2020); Photutils (Bradley et al. 2016); Interferopy (Boogaard et al. 2021); Astroquery (Ginsburg et al. 2019), and mpdaf (Bacon et al. 2016).

References

- Alcalde Pampliega, B., Pérez-González, P. G., Barro, G., et al. 2019, *ApJ*, 876, 135
- Amôres, E. B., Sodr , L., Minniti, D., et al. 2012, *AJ*, 144, 127
- Astropy Collaboration (Robitaille, T. P., et al.) 2013, *A&A*, 558, A33
- Astropy Collaboration (Price-Whelan, A. M., et al.) 2022, *ApJ*, 935, 167
- Bacon, R., Accardo, M., Adjali, L., et al. 2010, in *Ground-Based and Airborne Instrumentation for Astronomy III*, eds. I. S. McLean, S. K. Ramsay, & H. Takami, *SPIE Conf. Ser.*, 7735, 773508
- Bacon, R., Piqueras, L., Conseil, S., Richard, J., & Shepherd, M. 2016, *Astrophysics Source Code Library* [record ascl:1611.003]
- Bakx, T. J. L. C., & Dannerbauer, H. 2022, *MNRAS*, 515, 678
- Barnard, V. E., Vielva, P., Pierce-Price, D. P. I., et al. 2004, *MNRAS*, 352, 961
- Bernard, D. A., Yun, M. S., Harrington, K. C., et al. 2022, *MNRAS*, 515, 3911
- B thermin, M., Daddi, E., Magdis, G., et al. 2015, *A&A*, 573, A113
- Boogaard, L., Meyer, R. A., & Novak, M. 2021, <https://doi.org/10.5281/zenodo.5775604>
- Bouwens, R. J., Smit, R., Schouws, S., et al. 2022, *ApJ*, 931, 160
- Bradley, L., Sipocz, B., Robitaille, T., et al. 2016, *Astrophysics Source Code Library* [record ascl:1609.011]
- Buchner, J., Georgakakis, A., Nandra, K., et al. 2014, *A&A*, 564, A125
- Burgarella, D., Theul , P., Buat, V., et al. 2023, *A&A*, 671, A123
- Burgasser, A. J., Bezanson, R., Labbe, I., et al. 2024, *ApJ*, 962, 177
- Capak, P. L., Carilli, C., Jones, G., et al. 2015, *Nature*, 522, 455
- Carilli, C. L., & Walter, F. 2013, *ARA&A*, 51, 105
- Carniani, S., Ferrara, A., Maiolino, R., et al. 2020, *MNRAS*, 499, 5136
- CASA Team, Bean, B., Bhatnagar, S., et al. 2022, *PASP*, 134, 114501
- Casey, C. M., Narayanan, D., & Cooray, A. 2014, *Phys. Rep.*, 541, 45
- Chabrier, G. 2003, *PASP*, 115, 763
- Chapman, S. C., Smail, I., Blain, A. W., & Ivison, R. J. 2004, *ApJ*, 614, 671
- Chen, C.-C., Liao, C.-L., Smail, I., et al. 2022, *ApJ*, 929, 159
- Clements, D. L., Cairns, J., Greenslade, J., et al. 2024, *MNRAS*, 533, 4045
- Cox, P., Neri, R., Berta, S., et al. 2023, *A&A*, 678, A26
- da Cunha, E., Groves, B., Walter, F., et al. 2013, *ApJ*, 766, 13
- Daddi, E., Dannerbauer, H., Liu, D., et al. 2015, *A&A*, 577, A46
- De Looze, I., Cormier, D., Lebouteiller, V., et al. 2014, *A&A*, 568, A62
- D az-Santos, T., Armus, L., Charmandaris, V., et al. 2013, *ApJ*, 774, 68
- Dowell, C. D., Conley, A., Glenn, J., et al. 2014, *ApJ*, 780, 75
- Downes, D., & Solomon, P. M. 1998, *ApJ*, 507, 615
- Dunne, L., Maddox, S. J., Papadopoulos, P. P., Ivison, R. J., & Gomez, H. L. 2022, *MNRAS*, 517, 962
- Duplancic, F., Alonso, S., Coldwell, G., et al. 2024, *A&A*, 682, A153
- Dye, S., Furlanetto, C., Dunne, L., et al. 2018, *MNRAS*, 476, 4383
- Erickson, N. R., & Grosslein, R. M. 2007, *IEEE Trans. Microw. Theory Tech.*, 55, 2495
- Foreman-Mackey, D., Hogg, D. W., Lang, D., & Goodman, J. 2013, *PASP*, 125, 306
- Ginsburg, A., Sip cz, B. M., Brasseur, C. E., et al. 2019, *AJ*, 157, 98
- Goldreich, P., & Kwan, J. 1974, *ApJ*, 191, 93
- Greenslade, J., Aguilar, E., Clements, D. L., et al. 2019, *MNRAS*, 490, 5317
- Greenslade, J., Clements, D. L., Petitpas, G., et al. 2020, *MNRAS*, 496, 2315
- Gullberg, B., De Breuck, C., Vieira, J. D., et al. 2015, *MNRAS*, 449, 2883
- G sten, R., Nyman, L.  ., Schilke, P., et al. 2006, *A&A*, 454, L13
- Hainline, K. N., Helton, J. M., Johnson, B. D., et al. 2024, *ApJ*, 964, 66
- Harrington, K. C., Yun, M. S., Cybulski, R., et al. 2016, *MNRAS*, 458, 4383
- Harrington, K. C., Weiss, A., Yun, M. S., et al. 2021, *ApJ*, 908, 95
- Hern n-Caballero, A., P rez-Fournon, I., Hatziminaoglou, E., et al. 2009, *MNRAS*, 395, 1695
- Herrera-Camus, R., Sturm, E., Graci -Carpio, J., et al. 2018, *ApJ*, 861, 95
- Heyminck, S., Kasemann, C., G sten, R., de Lange, G., & Graf, U. U. 2006, *A&A*, 454, L21
- Hirashita, H., Ferrara, A., Dayal, P., & Ouchi, M. 2014, *MNRAS*, 443, 1704
- Hughes, D. H., J uregui Correa, J.-C., Schloerb, F. P., et al. 2010, in *Ground-Based and Airborne Telescopes III*, eds. L. M. Stepp, R. Gilmozzi, & H. J. Hall, *SPIE Conf. Ser.*, 7733, 773312
- Hunter, J. D. 2007, *Comput. Sci. Eng.*, 9, 90
- Ivison, R. J., Lewis, A. J. R., Weiss, A., et al. 2016, *ApJ*, 832, 78
- Jarugula, S., Vieira, J. D., Weiss, A., et al. 2021, *ApJ*, 921, 97
- Jin, S., Daddi, E., Magdis, G. E., et al. 2022, *A&A*, 665, A3
- Kraan-Korteweg, R. C. 2005, *Rev. Mod. Astron.*, 18, 48
- Kraan-Korteweg, R. C., & Lahav, O. 2000, *A&ARv*, 10, 211
- Krumholz, M. R., McKee, C. F., & Klein, R. I. 2005, *Nature*, 438, 332
- Lagache, G., Cousin, M., & Chatzikos, M. 2018, *A&A*, 609, A130
- Liu, D., Daddi, E., Schinnerer, E., et al. 2021, *ApJ*, 909, 56
- Lutz, D., Berta, S., Contursi, A., et al. 2016, *A&A*, 591, A136
- Maresca, J., & Dye, S. 2025, *MNRAS*, 537, 2708
- Maresca, J., Dye, S., Amvrosiadis, A., et al. 2022, *MNRAS*, 512, 2426
- McMullin, J. P., Waters, B., Schiebel, D., Young, W., & Golap, K. 2007, in *Astronomical Data Analysis Software and Systems XVI*, eds. R. A. Shaw, F. Hill, & D. J. Bell, *ASP Conf. Ser.*, 376, 127
- Narayanan, D., & Krumholz, M. R. 2014, *MNRAS*, 442, 1411
- Negrello, M., Amber, S., Amvrosiadis, A., et al. 2017, *MNRAS*, 465, 3558
- Neri, R., Cox, P., Omont, A., et al. 2020, *A&A*, 635, A7
- Nightingale, J. W., & Dye, S. 2015, *MNRAS*, 452, 2940
- Nightingale, J. W., Dye, S., & Massey, R. J. 2018, *MNRAS*, 478, 4738
- Nonino, M., Glazebrook, K., Burgasser, A. J., et al. 2023, *ApJ*, 942, L29
- Oke, J. B., & Gunn, J. E. 1983, *ApJ*, 266, 713
- Papadopoulos, P. P. 2010, *ApJ*, 720, 226
- Rangwala, N., Maloney, P. R., Glenn, J., et al. 2011, *ApJ*, 743, 94
- Reuter, C., Vieira, J. D., Spilker, J. S., et al. 2020, *ApJ*, 902, 78

- Reuter, C., Spilker, J. S., Vieira, J. D., et al. 2023, *ApJ*, **948**, 44
- Rosenberg, M. J. F., van der Werf, P. P., Aalto, S., et al. 2015, *ApJ*, **801**, 72
- Rygl, K. L. J., Benedettini, M., Schisano, E., et al. 2013, *A&A*, **549**, L1
- Santamaría-Miranda, A., de Gregorio-Monsalvo, I., Plunkett, A. L., et al. 2021, *A&A*, **646**, A10
- Schaerer, D., Ginolfi, M., Béthermin, M., et al. 2020, *A&A*, **643**, A3
- Schleicher, D. R. G., Spaans, M., & Klessen, R. S. 2010, *Highlights Astron.*, **15**, 426
- Schouws, S., Stefanon, M., Bouwens, R., et al. 2022, *ApJ*, **928**, 31
- Schreiber, C., Elbaz, D., Pannella, M., et al. 2018, *A&A*, **609**, A30
- Scoville, N. Z., & Kwan, J. 1976, *ApJ*, **206**, 718
- Scoville, N., Lee, N., Vanden Bout, P., et al. 2017, *ApJ*, **837**, 150
- Scoville, N., Faisst, A., Weaver, J., et al. 2023, *ApJ*, **943**, 82
- Sérsic, J. L. 1963, *Boletín de la Asociación Argentina de Astronomía La Plata Argentina*, **6**, 41
- Soto, K. T., Lilly, S. J., Bacon, R., Richard, J., & Conseil, S. 2016, *MNRAS*, **458**, 3210
- Strandet, M. L., Weiss, A., Vieira, J. D., et al. 2016, *ApJ*, **822**, 80
- Strandet, M. L., Weiss, A., De Breuck, C., et al. 2017, *ApJ*, **842**, L15
- Tacconi, L. J., Genzel, R., & Sternberg, A. 2020, *ARA&A*, **58**, 157
- Tamura, Y., Kawabe, R., Shimajiri, Y., et al. 2015, *ApJ*, **808**, 121
- Tamura, Y., Taniguchi, A., Bakx, T. J. L. C., et al. 2025, *ApJ*, **981**, 51
- Urquhart, S. A., Bendo, G. J., Serjeant, S., et al. 2022, *MNRAS*, **511**, 3017
- Valentino, F., Daddi, E., Puglisi, A., et al. 2020, *A&A*, **641**, A155
- Valentino, F., Fujimoto, S., Giménez-Arteaga, C., et al. 2024, *A&A*, **685**, A138
- van der Werf, P. P., Isaak, K. G., Meijerink, R., et al. 2010, *A&A*, **518**, L42
- Vieira, J. D., Marrone, D. P., Chapman, S. C., et al. 2013, *Nature*, **495**, 344
- Virtanen, P., Gommers, R., Oliphant, T. E., et al. 2020, *Nat. Methods*, **17**, 261
- Wang, T., Schreiber, C., Elbaz, D., et al. 2019, *Nature*, **572**, 211
- Weiß, A., Downes, D., Neri, R., et al. 2007, *A&A*, **467**, 955
- Wilkins, S. M., Stanway, E. R., & Bremer, M. N. 2014, *MNRAS*, **439**, 1038
- Williams, C. C., Labbe, I., Spilker, J., et al. 2019, *ApJ*, **884**, 154
- Witstok, J., Smit, R., Maiolino, R., et al. 2022, *MNRAS*, **515**, 1751
- Witstok, J., Jones, G. C., Maiolino, R., Smit, R., & Schneider, R. 2023, *MNRAS*, **523**, 3119
- Woudt, P. A., Kraan-Korteweg, R. C., Cayatte, V., Balkowski, C., & Felenbok, P. 2004, *A&A*, **415**, 9
- Yang, C., Omont, A., Beelen, A., et al. 2016, *A&A*, **595**, A80
- Yang, C., Gavazzi, R., Beelen, A., et al. 2019, *A&A*, **624**, A138

Appendix A: ALMA archival data

The specifics of the ALMA archival data in the Lupus-I molecular cloud that allowed us to confirm the extragalactic nature of the background source in J154506 are presented in this appendix. Fig. A.1 showcases the unresolved and resolved emission in ALMA Bands 3, 6, and 7. Table A.1 provides details of the specific projects, the central sky frequencies, sensitivity, and resolution. Details on data reduction are provided in Section 3.1.

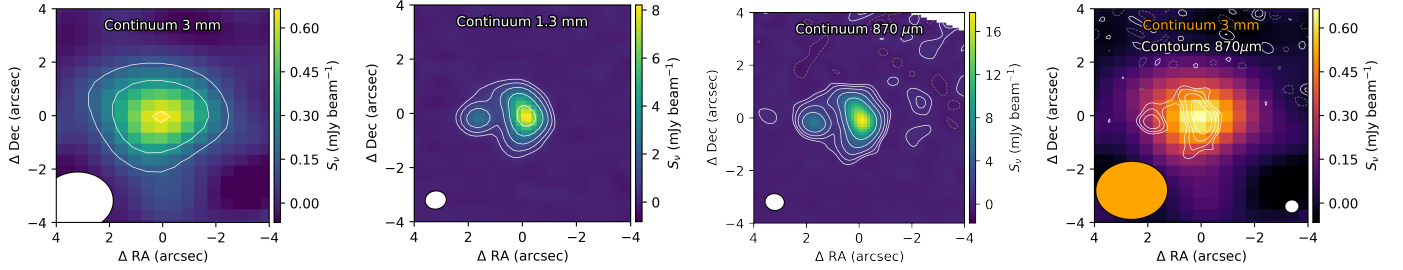


Fig. A.1. Left panels: 4'' \times 4'' ALMA Bands 3, 6, and 7 imaged with BRIGGS weighting (robust=0.5) centred on the gravitationally lensed galaxy J154506 are shown from left to right. -4, -2, 2, 4, 8, 16, and 32 σ contours are shown with solid and dashed white lines for positive and negative values, respectively. Right panel: Band 7 contours (BRIGGS weighting, robust=1.0) on top of the Band 3 data, for comparison purposes.

Table A.1. Overview of ALMA archival continuum observations for J154506.

	Cycle 3 B6	Cycle 5 B3 ^b	Cycle 6 B7	Cycle 7 B3	Cycle 8 B6
Project ID	2015.1.00512.S	gray2017.1.00303.S	2018.1.00126.S	2019.1.00245.S	2021.2.00097.S
Array	12m	12m	12m	12m	7m
Frequency [GHz]	216.1-234.4	93.1-107.3	333.1-348.7	93.1-107.3	216.0-234.5
Beam [arcsec ²] ^a	0.79'' \times 0.67''	—	0.88'' \times 0.75''	2.69'' \times 2.17''	6.47'' \times 4.22''
Spatial resolution [arcsec]	0.75	2.18	0.75	2.51	4.79
Sensitivity [mJy beam ⁻¹]	0.05	0.05	0.12	0.05	0.91

Notes. ^a The beam size corresponds to the imaging with BRIGGS weighting (robust=0.5). ^b In this work, we do not analyse Cycle 5 B3 semipass data, but details are shown in the table for completeness.

Appendix B: LMT spectral features

This appendix provides additional LMT/RSR zoomed spectra, supplementing the analysis presented in the main text and Figure 3.

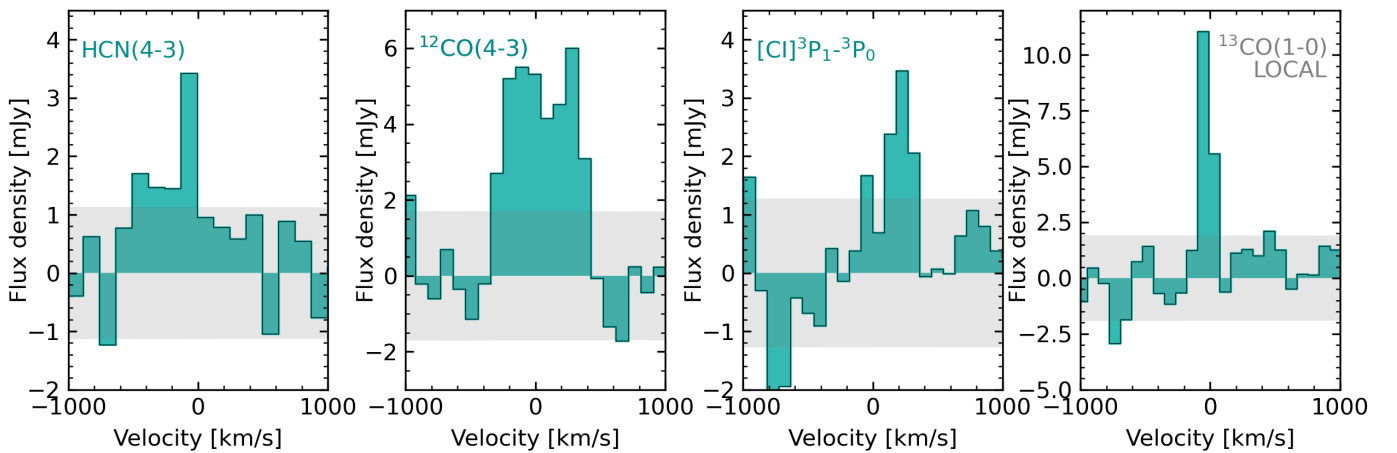


Fig. B.1. LMT/RSR spectra at their native (unbinned) resolution at the position of the detected lines at $z = 3.5715$ (three first panels; HCN(4-3), $^{12}\text{CO}(4-3)$, and $[\text{CI}]^3\text{P}_1-^3\text{P}_0$ from left to right) and the Lupus molecular cloud (right panel; local $^{13}\text{CO}(1-0)$). Note that the peak flux density is slightly higher than for the binned spectrum shown in the bottom panel of Figure 3.

Appendix C: ACA spectral scans

This appendix presents the spectral scans obtained with the Atacama Compact Array (ACA). Figure C.1 displays the observed spectra in Band 3 (B3) and Band 4 (B4), along with an analysis of potential line identifications.

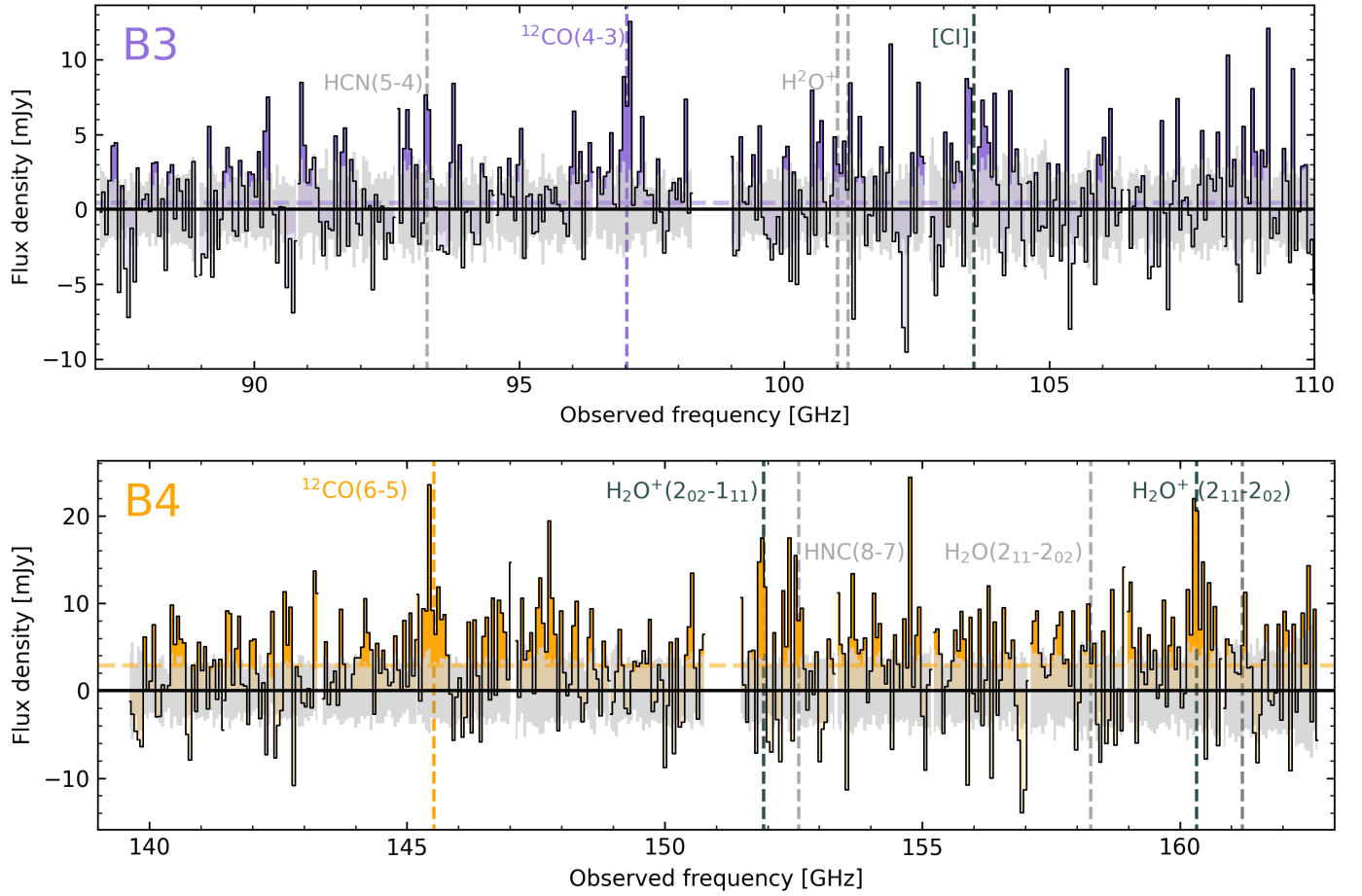


Fig. C.1. *Top panels:* ALMA/ACA B3 (*first row*, purple) and B3 (*second row*, orange) spectrum of J154506 (colour) and associated errors (grey) before continuum subtraction. The transitions above $S/N=5$ and 3 compatible with J154506's redshift ($z = 3.7515$) are marked with vertical dashed lines, and labelled in colour, and dark grey, respectively. Other $S/N>1$ consistent tentative transitions are highlighted in light grey. The medium continuum emission is highlighted with a coloured horizontal dashed line. *Bottom panels:* Continuum subtracted spectra at the position of the $S/N>3$ detected lines at $z = 3.7515$ in B3 (*left panels*; $^{12}\text{CO}(4-3)$, and $[\text{CI}]^3\text{P}_1-^3\text{P}_0$) and B4 (*right panels*; $^{12}\text{CO}(4-3)$, and $\text{H}_2\text{O}^+(2_{11}-2_{02})_{(3/2-3/2)}$).

Table C.1. Overview of ALMA/ACA spectral observations of J154506

Project ID	2023.1.00251.S (Cycle 10, ACA)					
Scan	B3a	B3b	B3c	B4a	B4b	B4c
Frequency, LSB [GHz]	87.0-90.8	90.8-94.5	94.5-98.3	139.6-143.3	143.3-147.1	147.1-150.8
Frequency, USB [GHz]	98.9-102.7	102.7-106.4	106.4-110.2	151.5-155.2	155.2-158.9	158.9-162.7
Beam [arcsec ²]	18.9'' × 8.9''	18.6'' × 8.7''	20.0'' × 8.4''	11.0'' × 6.5''	12.1'' × 5.7''	11.3'' × 5.3''
Spatial resolution [arcsec]	11.22	10.90	12.07	7.46	7.01	5.64
Sensitivity [mJy beam ⁻¹]	0.23	0.26	0.23	0.34	0.33	0.37
Spectral resolution [km s ⁻¹] ^a	12	3	3	2	2	2

Notes. ^aNote that this is the native spectral resolution, but spectral windows were binned to ≈ 100 km s⁻¹ to increase sensitivity as detailed in Section 3.2.

Appendix D: Photometry

This Appendix contains the archival and new photometric measurements used throughout this work.

Table D.1. Photometry (in mJy) used in this work to derive the physical properties of J154506.

Telescope/ instrument	Band (μ m)	Flux density (mJy)	Ref.	Telescope/ instrument	Band (μ m)	Flux density (mJy)	Ref.
MUSE	0.48-0.93	$(0.6 \pm 0.2) \times 10^{-3}$	This work	SMA	1300	20.8 ± 1.9	(1)
MIPS	24	<0.3	(1) ^a	ACA B4c	1940	4.9 ± 1.4	This work
SPIRE	250	40.9 ± 12.7	(1)	ACA B4b	1980	4.8 ± 1.5	This work
SPIRE	350	109.4 ± 11.4	(1)	ACA B4a	2030	3.8 ± 1.2	This work
SPIRE	500	134.9 ± 11.9	(1)	ACA B3c	2930	1.1 ± 0.4	This work
SMA	890	69.7 ± 12.1	(1)	ALMA B3	3000	0.9 ± 0.2	This work
ALMA B7	890	46.5 ± 3.7	This work	ACA B3b	3040	0.8 ± 0.3	This work
AzTEC	1100	43.9 ± 5.6	(1)	ACA B3a	3160	0.3 ± 0.2	This work
ALMA B6	1300	21.3 ± 1.8	This work	ATCA	7000	$210 \pm 35 \times 10^{-3}$	(1)
ACA B6	1300	18.0 ± 4.4	This work	VLA	60000	$66 \pm 5 \times 10^{-3}$	(1)

Notes. ^a For archival multi-wavelength data we refer the reader to the details provided in Tamura et al. 2015 (1).

Appendix E: Simultaneous modelling of the observed continuum and emission lines

The TUNER model solves for the non-LTE radiative transfer of the lines in the LVG approximation and effectively computes the line brightness temperatures by simultaneously fitting the dust continuum and line emission. The dust temperature and continuum emission serves as an additional temperature floor on top of the blackbody CMB radiation at the redshift of the object. We additionally constrain the parameter space by implementing a physically motivated range of the $T_{\text{kin}}/T_{\text{dust}}$, and couple the H₂ density and gas kinetic temperature with a power-law slope index. Still, there can be a wide-ranging and highly degenerate parameter space. We have applied the Markov chain Monte Carlo *emcee* Python package (Foreman-Mackey et al. 2013) using 100 walkers and 50 autocorrelation times and uniform priors.

Here we have allowed the following parameters to be optimized and show their 1D and 2D marginalized posterior distributions: dust temperature and dust emissivity index T_{dust} (K) and β_{dust} , gas kinetic temperature T_{kin} (K), turbulent velocity dispersion ΔV (km s⁻¹), emitting size radius r (pc), $\log(n(\text{H}_2))$ [cm⁻³], and gas kinetic temperature to density power law slope (β_{T}) which couples the gas kinetic temperature to the gas volume density by a power-law index, $\beta_{\text{T,kin}}$, as $T_{\text{kin}} \propto \log(n(\text{H}_2))^{\beta_{\text{T,kin}}}$, such that the more diffuse gas tends to have higher gas kinetic temperatures. The magnification of the object (see Section 5) is fixed in the model to therefore provide the intrinsic source properties (see Weiß et al. 2007).

Table E.1. Parameter space explored by our *Turbulence* model

$T_{\text{kin}}/T_{\text{dust}}$	ΔV [km s ⁻¹]	γ_T	β_{dust}	r [kpc]	T_{kin} [K]	$\log(n(\text{H}_2))$ [cm ⁻³]
0.5—6	1—150	-0.3—0.005	1.5—2.8	0.1—8000	T_{CMB}^a —600	1—7

Notes. ^aThe minimum temperature is the temperature of the CMB at $z=3.75$ plus a temperature floor of 10K.

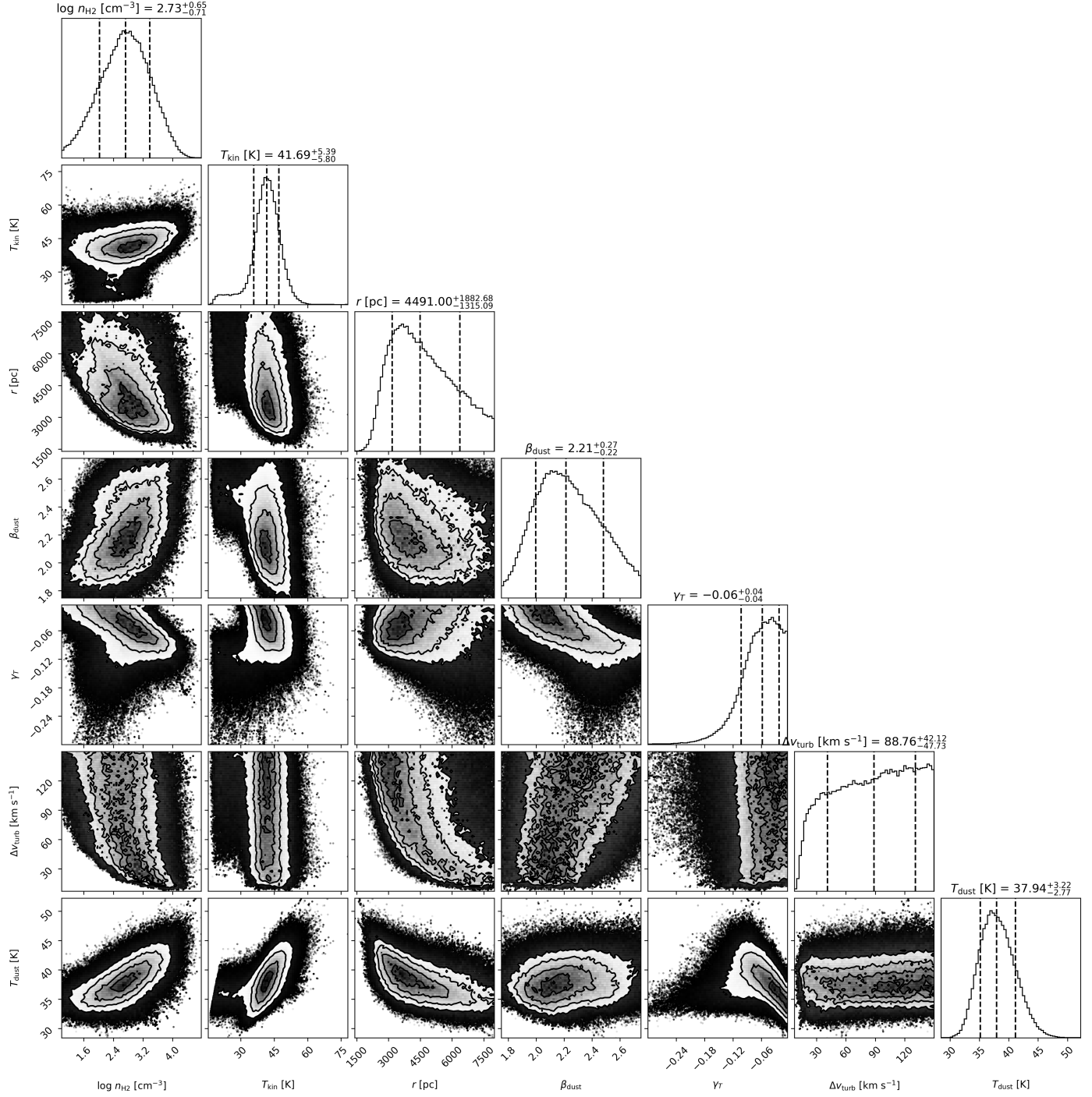


Fig. E.1. Derived marginalized 1D and 2D posterior distributions for H₂ gas density $\log(n(\text{H}_2))$, gas kinetic temperature (T_{kin}), emitting radius (r), dust emissivity index (β_{dust}), density-to-gas kinetic temperature power-law slope index (γ_T), turbulent velocity dispersion (ΔV), and dust temperature (T_{dust}) are shown. Note that the gas density is in log10 units. The $\log([\text{CO}]/[\text{H}_2])$ and GDMR are fixed to -4.0 and 150, respectively.

Appendix F: MERCURIUS FIR FIT

This appendix provides the posterior distribution of the main parameters considered by MERCURIUS during the FIR fitting and dust properties estimation process for both the self-consistent and the entirely optically thin scenario.

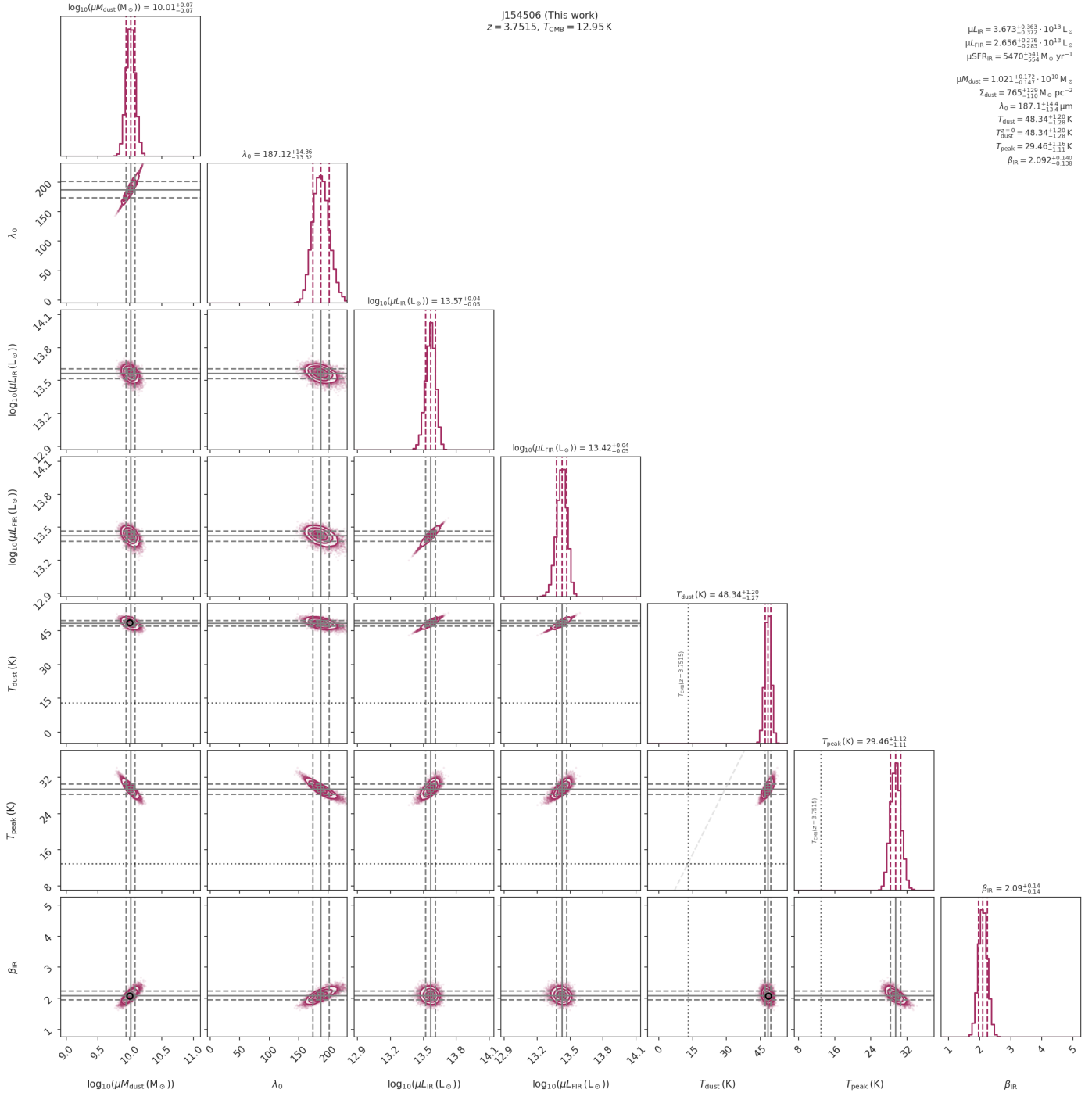


Fig. F.1. Corner plot of the posterior distribution obtained from the MERCURIUS FIR fitting for J154506 at $z = 3.7515$ shown in Fig. 6 before correcting for magnification under a self-consistent scenario. Derived values for the dust mass (M_{dust}), opacity transition wavelength (λ_0), dust temperature (T_{dust}), and dust emissivity index (β_{IR}) are shown. Solid grey lines indicate the median (i.e. 50th percentile) of the parameter's marginalised posterior distribution, while dashed lines show the 16th and 84th percentiles. In panels with the dust temperature, a dotted line indicates T_{CMB} at the redshift of J154506 ($T_{CMB} = 12.95$ K). We note that the total IR luminosity (L_{IR}) is not an independent parameter of the fitting routine, and is included purely for visualisation purposes.

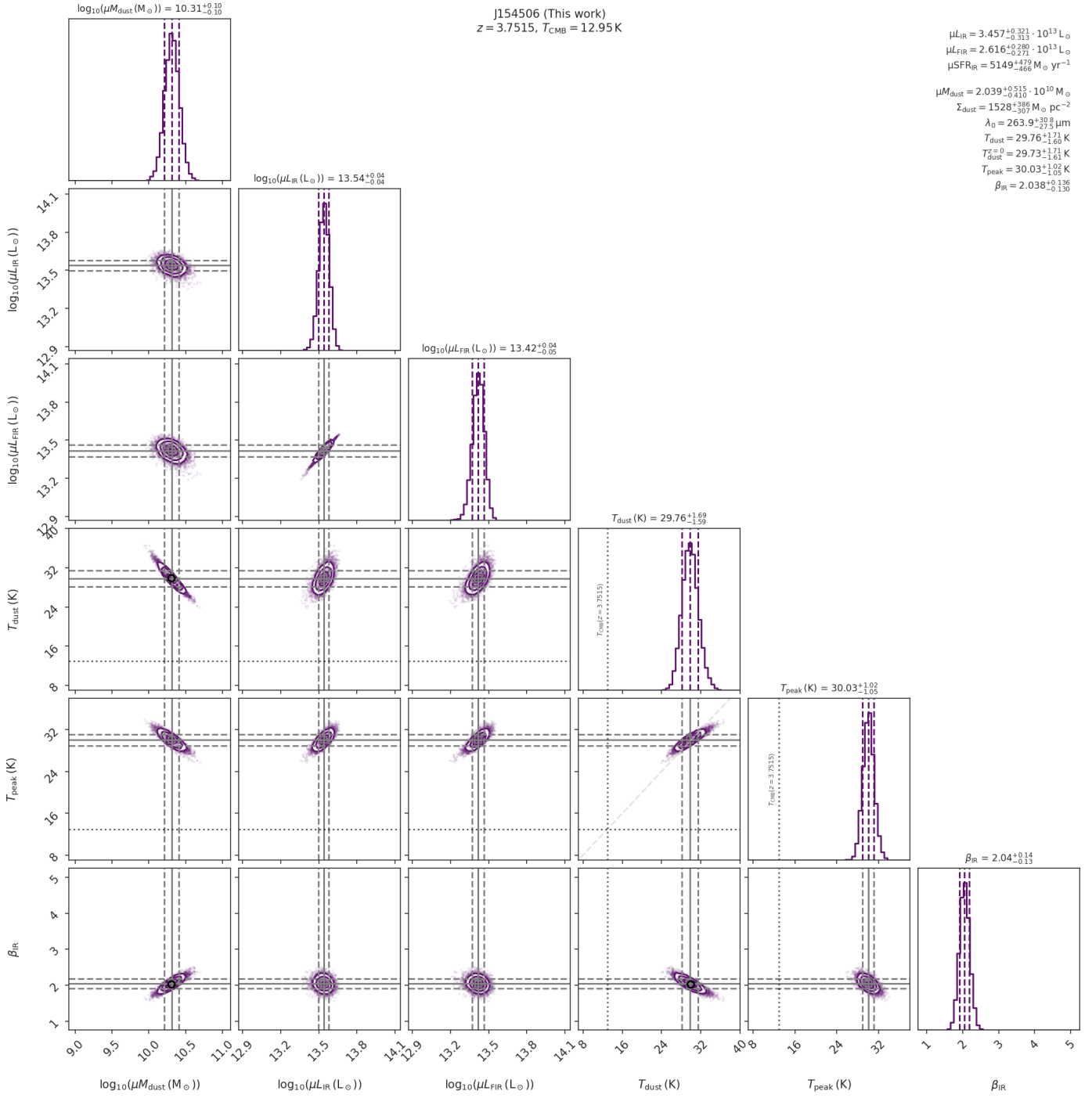


Fig. F2. Corner plot of the posterior distribution obtained from the MERCURIUS FIR fitting for J154506 at $z = 3.7515$ assuming an optically thin scenario.